# Experimental Determination of the Speciation, Partitioning, and Release of Perrhenate as a Chemical Surrogate for Pertechnetate from a Sodalite-Bearing Multiphase Ceramic Waste Form

**E.M. Pierce[*1], W.W. Lukens[2], J.P. Fitts[3], G. Tang[1], and C.M. Jantzen[4]**

[1]Ennvironmental Sciences Division, Oak Ridge National Laboratory, Oak Ridge, TN 37831
[2]Chemical Sciences Division, Lawrence Berkley National Laboratory, Berkeley, CA 94720
[3] Department of Civil and Environmental Engineering, Princeton University, Princeton, NJ 08544
[4]Savannah River National Laboratory, Aiken, SC 29808
[*]Corresponding Author: E-mail: pierceem@ornl.gov, Phone: (865) 574-9968, Fax: (865) 576-8646,

**Abstract**

Multiphase ceramic waste forms have been studied extensively as a potential host matrix for nuclear waste. Understanding the speciation, partitioning, and release behavior of radionuclides immobilized in multiphase ceramic waste form is critical when developing the scientific and technical basis for nuclear waste management. In this study, we evaluated a sodalite-bearing multiphase ceramic waste form (i.e., fluidized-bed steam reform sodium aluminosilicate [FBSR NAS]) as a potential host matrix for long-lived radionuclides, such as technetium ($^{99}$Tc). The FBSR NAS material consists primarily of nepheline (ideally $NaAlSiO_4$), anion-bearing sodalites (ideally $M_8[Al_6Si_6O_{24}]X_2$, where M refers to is alkali and alkaline earth cations and X refers to monovalent anions), and nosean (ideally $Na_8[AlSiO_4]_6SO_4$). Bulk x-ray absorption fine structure analysis of the multiphase ceramic waste form, suggest rhenium (Re) is in the Re(VII) oxidation state and has partitioned to a Re-bearing sodalite phase (most likely a perrhenate sodalite $Na_8[Al_6Si_6O_{24}](ReO_4)_2$). In this study Re was added as a chemical surrogate for $^{99}$Tc during the waste form synthesis process. The weathering behavior of the multiphase ceramic waste form was evaluated under hydraulically unsaturated conditions with deionized water at 90°C. The steady-state Al, Na, and Si concentrations suggests the weathering mechanisms are consistent with what has been observed for other aluminosilicate minerals and include ion exchange, network hydrolysis, and formation of enriched-silica surface layer or phase. Ion exchange is evident by the average Na normalized release being 2.3 times greater than Al. Matrix dissolution is evident by the XRD depth dependent alteration phase profile and the steady-state Al concentration being consistent with nepheline solubility. Silica-rich surface layer or phase formation is evident by the steady-state Si concentrations being consistent with the solubility of amorphous $SiO_2$ or chalcedony. The steady-state S and Re concentrations are within an order of magnitude of the nosean and perrhenate sodalite solubility, respectively. The order of magnitude difference between the observed and predicted concentration for Re and S may be associated with the fact that the anion-bearing sodalites contained in the multiphase ceramic matrix are present as mixed-anion sodalite phases. Lastly, a comparison of the results discussed in this study to data previously collected on Hanford low-activity waste (LAW) glass indicates that Re release from the multiphase ceramic matrix is either an order of magnitude lower or 6 times faster to $^{99}$Tc release from LAW glass depending on whether the BET or geometric surface area is used to normalize the Re release rates.

**Keywords:** Ceramic Waste Forms; Sodalite Technetium; Rhenium; Nuclear Waste; Pressurized Unsaturated Flow

## 1 Introduction

Feldspathoid and zeolites, such as sodalite (general formula of $M_8[Al_6Si_6O_{24}]X_2$, where M is an alkali cation—such as Cs, K, Na, etc—and X is a monovalent anion, such as $Br^-$, $Cl^-$, $I^-$, $TcO_4^-$, $ReO_4^-$, $SO_4^{2-}$, etc.), are a large and diverse classes of minerals characterized by a crystalline framework of tetrahedral Al and Si with a three-dimensional pore system that can accommodate a variety of anions (Brenchley and Weller, 1994; Buhl et al., 2001; Buhl et al., 1989; Campbell et al., 2000; Deer et al., 1963; Fechtelkord, 2000; Gesing and Buhl, 1998; Johnson et al., 2000; Mattigod et al., 2006; Shannon et al., 2000; Srdanov et al., 1994; Zhao et al., 2004). The common theme in sodalite group minerals is the flexible framework structure that can expand to enclathrate various guest anions by cooperative changes in the Al-O-Si bond angle (Pauling, 1930). The synthesis and stability under laboratory and hydrothermal conditions have been studied extensively because of the importance of zeolite-type phases as industrial catalysts and molecular sieves. Additionally, these phases have been postulated to form in the environment at locations where the unintentional release of caustic, high ionic strength, Al-rich waste solutions that exceed 60°C have reacted with subsurface sediments; which consist mainly of quartz, feldspar, hornblende, mica, chlorite, illite, kaolinite, smectite, and calcite (Serne et al., 1998), at the Hanford site in Richland, WA (Bickmore et al., 2001; Chorover et al., 2003; Deng et al., 2006a; Deng et al., 2006b; Mashal et al., 2004; Mon et al., 2005; Qafoku et al., 2003a; Qafoku et al., 2003b; Rivera et al., 2011; Zachara et al., 2007; Zhao et al., 2004).

In addition to industrial applications and presence in contaminated systems, sodalite group minerals have been studied by a number of investigators as a potential host media for the immobilization of defense high-level waste (HLW), commercial nuclear waste, and transactinide elements, such as plutonium, in multiphase ceramic waste forms (Barney, 1974; Fanning et al., 2003; Hatch, 1953; Hench et al., 1981; Hench et al., 1986; Moschetti et al., 2000; Sinkler et al., 2000). For example, a glass-bonded sodalite has been considered as a host matrix for the disposal of electrorefiner wastes from sodium-bonded metallic spent nuclear fuel removed from the EBR II fast breeder reactor (Fanning et al., 2003; Moschetti et al., 2000; Sinkler et al., 2000). In this paper we evaluate the potential for a sodalite-bearing multiphase ceramic waste form (i.e., fluidized-bed steam reformer sodium aluminosilicate granular product [FBSR NAS]) to resist aqueous corrosion and retain key risk driving radionuclides (e.g., technetium-99 [$^{99}Tc$]). The FBSR NAS waste form is primarily composed of nepheline (ideally $NaAlSiO_4$), anion-bearing sodalites (ideally $Na_8[AlSiO_4]_6Cl_2$), and nosean (ideally $Na_8[AlSiO_4]_6SO_4$).

Multiphase ceramic waste forms have been studied extensively as a potential host matrix for radionuclides (Lumpkin, 2006; Stefanovsky et al., 2004). Some of the most studied multiphase waste forms include the multiple versions of SYNthetic ROCk (SYNROC) (Ringwood et al., 1978), tailored ceramics (Harker, 1988), pyrochlore (Icenhower et al., 2006; Weber et al., 1986), zirconolite (Clinard et al., 1984a; Clinard et al., 1984b), and glass-ceramics (O'Holleran et al., 1997). For an overview of the state-of-the-science on the afore-mentioned multiphase waste forms see the reviews by Lutze and Ewing (1988), Lee et al. (2006), Caurant et al. (2009), and NRC (2011). Improving the scientific and technical basis for using each of the different types of multiphase ceramic waste forms in nuclear waste management requires an understanding of the speciation, partitioning, and the release behavior of radionuclides immobilized in the multiphase matrix.

In this study, we evaluate the FBSR NAS ceramic waste form for Hanford low-activity waste (LAW) immobilization by providing insight into the speciation, partitioning and release behavior of Re. The perrhenate ($ReO_4^-$) ion was added to the LAW simulant as a chemical analogue for the pertechnetate ($TcO_4^-$) ion during the synthesis of the FBSR NAS granular product. The volume of immobilized LAW at Hanford is the largest in the DOE complex and is one of the largest inventories (approximately $8.9 \times 10^{14}$ Bq total activity) of long-lived radionuclides, principally $^{99}Tc$ ($t_{1/2} = 2.1 \times 10^5$), planned for disposal in a near-surface burial facility (Mann, 2003). Vitrification at the Hanford Waste Treatment and Immobilization Plant (WTP) represents the baseline treatment approach for the LAW stream (ORP, 2011). However, the treatment capacity at WTP is not sufficient for the estimated volume of LAW and it is anticipated that a supplemental technology, such as the FBSR NAS waste form or equivalent material, will be required to meet project goals (DOE, 2012; ORP, 2011). The objective of the experiments discussed in this manuscript was to determine for the first time the oxidation state, speciation, and mineral association for the rhenium (Re) in the FBSR NAS waste form matrix. In addition to determining the Re speciation in the FBSR NAS waste form, a 2.5-year long weathering experiment was conducted under hydraulically unsaturated conditions with the goal of determining (1) the alteration phase or phases that form as a result of long-term weathering, (2) the evolution in the solution chemistry that occurs during the multiphase wasteform-water interaction, and (3) to gain insight into the $ReO_4^-$ release mechanism, as a chemical analogue to $TcO_4^-$.

## 2 Material Production and Characterization

### *2.1 Description of the fluidized-bed steam reformer production process*

The THermal Organic Reduction (THOR$^{SM}$) Treatment Techologies (TTT) Fluidized-Bed Steam Reformation (FBSR) process operates by introducing high sodium nitrate content tank wastes into a moderate temperature (650 – 800°C) fluidized bed. The tank waste is reacted with carbon and iron-based reductants to covert nitrates and nitrites directly to nitrogen gas. Radionuclides, alkali metals, sulfate, chloride, fluoride, and non-volatile heavy metals in the waste stream are reacted with clay (kaolinite) or other inorganic materials to produce a polycrystalline mineral product. For additional details on THOR-TTT FBSR process see Jantzen (2002), Olson et al. (2004), Soelberg et al. (2004), or visit the THOR$^{SM}$–TTT website (www.thortt.com).

### *2.2 Synthesis and composition*

In August 2004, a pilot-scale test of THOR Treatment Technology mineralized FBSR process technology was conducted at the SAIC STAR facility at INEEL. The results of the pilot-scale tests conducted with the externally heated 6-inch reformer system is described in Olson et al. (2004). The pilot-scale run was terminated on August 5, 2004, and resulted in a continuous operating time (COT) of 68 hours and 26 minutes (68:43 hours) with a LAW slurry feed rate that ranged from 3 to 5.5-kg/hour. The FBSR LAW 1104/1123 sample used to produce the test results discussed below represents a sample of the bed product removed at 55:30 hours of the COT cycle. The FBSR LAW 1125 filter fines were also removed during this time period and represent the final filter fines. The additives used to produce the mineralized product include the Hanford LAW simulant, starting bed media, carbon reductive additive, and mineralized additive. The Hanford LAW simulant, which primarily consist of sodium and potassium salts, used in this pilot-scale test was a six-tank composite sample designed to represent dissolved radioactive saltcake (Mahoney and Rassat, 2003; Olson et al., 2004). The purpose of the starting bed material was to facilitate heat transfer to the atomized feed and prevent over-quenching in the feed zone. A wood-based carbon received from Berger Brothers of Chicago was used as the reductive additive in this test. Carbon was added to the system to provide heat input to the bed and to form reducing conditions for nitrogen oxides destruction. The mineralized clay additive used was OptiKasT clay, which consists mainly of kaolinite ($Al_2O_3$•$2SiO_2$•$2H_2O$) with a minor amount of muscovite $[(K,Na)(Al,Mg,Fe)_2(Si_{3.1}Al_{0.9})O_{10}(OH)_2$. The kaolin clay was added to provide sufficient reactive Al and Si to combine with alkali elements in the feed to produce nepheline and other aluminosilicate mineral phases in the reformer. The raw materials used to prepare the FBSR waste forms were characterized with respect to their chemical

composition. The results of these analyses and the approaches used to prepare the samples are discussed in Olsen et al. (2004) and Jantzen et al. (2004). The elemental composition of the raw solid materials as well as the final bed product (FBSR LAW 1104/1123) and filter fines (FBSR LAW 1125) are provided in Table 1.

*2.3 Test sample preparation and specific surface area measurement*

The as-received material was sieved into the 450 to 149 μm (<40 to >100 mesh) and 149 to 75 μm (<100 to >200 mesh) size fraction with standard ASTM sieves (ASTM, 2008). The sieved material was then washed in ethanol, washed again with ethanol in an ultrasonic bath, rinsed with ethanol, and then dried in a 90°C (±2°C) oven. Each sample before testing was stored at room temperature (~23°C) in a desiccator that contained $CaSO_4$.

Because of the limited amount of available material for the PUF experiments, the specific surface area for the 149 to 75μm size fraction was measured and used to estimate the surface area of the 450 to 149 μm sample. The specific surface area of the 149 to 75 μm was determined to be 4.15 ±0.01 $m^2/g$ with $N_2$-adsorption BET measurements using a Micromeritics ASAP 2010 surface area analyzer (Brunauer et al., 1938). This measurement was comparable to the value reported by Lourier et al. (2005) for the same size fraction and approximately two-times higher than the value for the SCT02-098 FBSR product reported by McGrail et al. (2003a; 2003b). For comparison, the geometric surface area for the 149 to 75 μm size fraction was estimated to be 0.02 $m^2/g$, with the geometric equation McGrail et al. (1997), Equation (1),

$$S_{GEO} = \frac{3}{\rho r} \tag{1}$$

where $S_{GEO}$ = surface area ($m^2/g$), $r$ = is the average radius of the particle (m), and $\rho$ = is the particle density ($g/cm^3$). The particle density, measured with an Accupyc 1330 He pycnometer, was determined to be 2.663 ±0.005 $g/cm^3$ and is comparable to the value of 2.764 ±0.004 $g/cm^3$ reported by McGrail et al. (2003a). Equation (1) assumes the grains are spherical and the sizes are normally distributed; surface pits, cracks, and other forms of surface roughness do not affect the surface area.

It is important to note that surface area has been recognized as an important factor in quantifying mineral dissolution rates. The proper handling of surface area is one of, if not the most problematic variable, and has been the subject of numerous studies (Brantley and Mellot, 2000). A large degree of uncertainty is associated with measurements of bulk BET surface area, and the contribution of actual reactive surface area is not always known. For glasses, it has been shown that the geometric surface area best represents the overall glass surface area (McGrail

et al., 1997) but no such case currently exists for the FBSR product. As previously discussed, two methods were used to determine the surface area of the FBSR product, calculated geometric (McGrail et al., 1997) and $N_2$-adsorption BET (Brunauer et al., 1938). A comparison of these values illustrates the calculated geometric surface area is 216 times less than the measured value via $N_2$-adsorption BET. In the case of glass, the geometric surface area is approximately two to five times less than the Kr-adsorption BET measurement and this difference has been attributed to the presence of a minor amount of smaller particles that remain adhered to the surface of the larger glass grains after washing (Pierce and Bacon, 2011; Pierce et al., 2007; Pierce et al., 2008).

As previously discussed in McGrail et al. (2003a), the FBSR product contains a large amount of microporosity that increases the reactive surface area (Fig. 1). A similar observation was also reported by Lorier et al. (2005) for the FBSR LAW 1123 bed material. Although use of the BET surface area may overestimate the true reactive surface area, the obvious microporosity indicates that use of the geometric surface area will underestimate the true dissolution rate. Therefore, the dissolution rates reported here have been normalized to the BET surface area. The true reactive surface area is probably less than the BET value, but also probably significantly higher than the geometric value. Additional work will be required to better constrain the reactive surface area of the FBSR product. Another factor that complicates the surface area estimates is the fact that the FBSR product is composed of several different mineral phases, each of which can have very different surface area measurements and therefore surface roughness factors. This also complicates the evaluation of the results because we cannot assign a specific values to any of the know phases that are present.

The calculated geometric surface area for the 450 to 149 μm sample that will be used in the PUF experiments was estimated to be 0.0078 $m^2/g$. Multiplying the surface roughness factor (216) by the geometric surface area results in an estimated $N_2$-BET surface area of 1.68 $m^2/g$ for the 450 to 149 μm. This value will be used to calculate elemental release rates from the PUF experiments.

*2.4 X-ray diffraction and Scanning Electron Microscopy*

Powder XRD patterns were recorded with Cu $K_\alpha$ radiation X-ray tube ($\lambda$= 1.54 Å) and data were collected in the $2\theta$ range: 2 to 65°, with a scanning step size of 0.02° $2\theta$ and a dwell time of 2 s. The data were analyzed with the computer program JADE (MDI, Livermore, California) combined with the Joint Committee on Powder Diffraction Standards (JCPDS) International Center for Diffraction Data (ICDD) (Newtown Square, Pennsylvania) database.

Upon termination of the experiment, the reacted solids were subsampled as found (loose and moist particles). The first 3.5-mm (i.e., vertical top) of the column, which represents the most reacted particles, was subsampled twice. The remaining length of the column (from top to bottom) was sampled as a function of depth (~6.5-mm intervals). The subsamples were placed in plastic vials, dried at room temperature in a sealed container with $CaSO_4$ desiccant, and analyzed for secondary reaction products with XRD.

Scanning electron microscopy (SEM) images were taken to determine particle morphology, size, and porosity of unreacted samples. Operating conditions were 20 keV for SEM imaging. Photomicrographs of high-resolution secondary electron images were obtained as digital images and stored in electronic format. The SEM mounts consisted of double-sided carbon tape attached to a standard aluminum planchet. The sample mounts were then carbon-coated via vacuum sputtering to improve the conductivity of the samples, and thus, the quality of the SEM images.

*2.5 X-ray absorption spectroscopy*

Bulk XAFS analysis was conducted by placing approximately 200 mg of unreacted sample in a Teflon holder sealed with Kapton tape. The bulk Re $L_{II}$-edge (11 959 eV) X-ray Absorption Near Edge Structure (XANES) spectra of the bed product (FBSR 1123) and filter fines (FBSR 1125) were collected in fluorescence at Stanford Synchrotron Radiation Lightsource (SSRL) on beamline 11-2. The beamline configuration consisted of a cryogenically cooled Si(220), ✱ = 90°, double-crystal monochromator with the second crystal detuned by 70% to reduce the harmonic content of the beam. Incident and transmitted beam intensity was determined using nitrogen filled ion chambers. Fluorescence data was collected with a Canberra 32 element germanium detector and are corrected for detector dead time. Data were normalized and corrected for self-absorption using Athena (Ravel, 2005)

### 2.5.1 Bulk Rhenium $L_{II}$-edge XAFS Reference Spectra and Data Analysis

Four reference spectra, $ReO_2$, $ReO_3$, $KReO_4$, and $ReO_4^-$-sodalite, were used for data fitting. The spectrum of $ReO_4^-$-sodalite (Pierce et al., submitted) was collected on SSRL beamline 11-2 and normalized as described above, except that the data were collected in transmission using nitrogen filled ion chambers. The other reference spectra have been described previously (Lukens et al., 2007). Data were fit using the program "fites," which performs a non-linear least squares fit of the data (http://lise.lbl.gov/RSXAP). XANES fitting was performed in a series of iterations. The XANES spectra of the FBSR 1123 and 1125 samples were initially fit using all of the reference spectra. If the contribution of any spectrum was smaller than its standard deviation, it was removed from the set of

standard spectra, and the fit was repeated. This process was repeated until the contribution of each remaining spectrum was greater than its standard deviation. In the end, only $KReO_4$, and $ReO_4^-$ sodalite contributed to the fit, which used five parameters: the contribution of each standard spectrum, a global energy shift, and a linear correction. Data were fit between 11940 and 12040 eV. Data resolution was 6 eV as determined from the white line for each of the measurements performed at the different beam lines, so the XANES spectrum contains 16.6 independent data points.

### 2.5.2 F-test for Rhenium $L_{II}$-edge results

The improvement to the fit due to the inclusion each reference spectrum in the final fit was determined using the F-test (Downward et al., 2007). Briefly, the data was fit using the final set of reference spectra to give the best fit. Then, the fit was repeated multiple times with the amplitude of one of the reference spectra set to zero each time, which produced a larger *r*-factor. For each component, *F* was determined using

$$F = \left( \frac{r_q^2 - r_0^2}{r_0^2} \right) \left( \frac{m - n}{b} \right) \tag{2}$$

where $r_q$ is the *r*-factor of a fit with the amplitude of 1 component set to zero, $r_0$ is the *r*-factor for the fit including all components, *m* is the number of independent data (16.6), *n* is the number of parameters in the best fit (5), and *b* is the difference between the number of parameter in the best fit and the number of parameters with one component set to zero (1). The probability (*p*) that a given value of *F* was due to random error was determined using Excel.

*2.6 Pressurized unsaturated flow (PUF) test*

The long-term weathering of nuclear waste forms has been studied for more than two decades. Although the results are useful, some of the alternative test methods (e.g., vapor hydration test [VHT], product consistency test [PCT-B],and unsaturated drip test [UDT]) have yielded data with limited applicability to the development of models that can accurately describe the underlying processes controlling the long-term elemental release rates under repository relevant conditions. See the Pierce et al. (2007; 2006) for a discussion of how the PUF test compares to other accelerated weathering experiments. Unlike the aforementioned methods, the PUF apparatus allows for accelerated weathering experiments to be conducted under hydraulically unsaturated conditions, thereby mimicking the open-flow and transport properties of the disposal system environment while accelerating the para-genetic transformation reactions the mineralized waste form is expected to undergo over time in a disposal facility. In the

PUF experiment, the paragenetic transformation reactions are accelerated by conducting experiments at temperatures that are above the 15°C disposal conditions and at high solid to solution ratios.

The PUF system and test procedure have been described previously by McGrail et al. (1999; 1996b; 2000) and Pierce et al. (2011; 2005; 2007; 2004; 2006), and only a general description is provided in this paper. The PUF system has a 7.62-cm long and 1.91-cm diameter column fabricated from a chemically inert material, polyetheretherketone (PEEK), so that dissolution reactions are not influenced by interaction with the column material. A porous Ti plate with a nominal pore size of 0.2-µm is sealed in the bottom of the column to ensure an adequate pressure differential for the conductance of fluid while operating under unsaturated conditions (Wierenga et al., 1993). Titanium is chosen because it is highly resistant to corrosion and has excellent wetting properties. Once the porous Ti plate is water saturated, water but not air is allowed to flow through the 0.2-Om pores, as long as the applied pressure differential does not exceed the air entry relief pressure, referred to as the bubble pressure, of the Ti plate. If the pressure differential is exceeded, air will escape through the plate and compromise the ability to maintain unsaturated flow conditions in the column. The computer control system runs LabVIEW➤(National Instruments Corporation) software for logging test data from several thermocouples, pressure sensors, inline sensors for effluent pH and conductivity, and from an electronic strain gauge that measures column mass to accurately track water mass balance and saturation level. The column also includes a PUF port, which is an electronically actuated valve that periodically vents the column gases. The purpose of column venting is to prevent reduction in the partial pressure of important gases, especially $O_2$ and $CO_2$, which may be consumed in a variety of chemical reactions.

The PUF column was packed with 14.79 g of crushed <40 to >100 mesh (from 450 to 149 Om particles) and cleaned FBSR LAW 1123 bed product, which resulted in a fill volume of 5.35 $cm^3$ and void volume of 15.56 $cm^3$. Finally the bottom 0.81 $cm^3$ of column volume was packed with crushed sapphire to provide a filter bed between the FBSR LAW 1123 bed product and the Ti porous plate. The filter bed was placed at the base of the column to minimize the entrapment of colloidal particles in the porous plate. The reader should note that in comparison to the mineral phases contained in the FBSR LAW 1123 product, sapphire, a high temperature $Al_2O_3$ mineral phase, is relatively corrosion resistant. In other words, sapphire will have a much slower corrosion rate and is considered to be relatively un-reactive; therefore, it is not expected to impact the results of this experiment. The mass difference between the packed and empty column was used to calculate the initial porosity of approximately 0.72 ±0.03 (unitless). After packing, the column was then vacuum saturated with 18M✳DIW at ambient temperature. A

temperature controller was then programmed to heat the column to 90°C (±1°C) in approximately 1 hr (1°C/min). The column initially was allowed to desaturate by gravity drainage during heating and was also vented periodically to maintain an internal pressure less than the bubble pressure of the porous plate. After reaching 90°C (±1°C), the influent valve was opened, and influent was set to a flow rate of 2 mL/d. The influent reservoir containing 18 MΩ DIW was maintained at ambient temperature and periodically refilled during the test. Column venting was set to occur once an hour, so the partial pressure of $O_2$ and $CO_2$ could remain relatively constant. Effluent samples were collected into tared vials from which samples were extracted and acidified for elemental analysis with inductively coupled plasma-optical emission spectroscopy (ICP-OES) and -mass spectrometry (ICP-MS).

*2.7 Effluent solution analyses*

All effluent solutions were monitored for pH and electrical conductivity with in-line sensors. Prior to starting the experiments, the in-line pH probe was calibrated with NBS buffers (pH = 7.00, 10.00, or 12.00 at 25°C). Precision of pH measurement was ±0.05 pH units. The in-line Pharmacia Biotech electrical conductivity sensor was calibrated with a freshly made solution of 1.0 M NaCl. The 1.0 M NaCl solution was prepared by adding 11.67 g of analytical grade NaCl powder to 200 mL of 18 MΩ DIW. Concentrations of Re in effluent solution samples were determined with ICP-MS methods; whereas concentrations of Al, Cr, Fe, K, Na, Si, Ti, and Zr were determined with ICP-OES methods. After passing through the 0.2-μm Ti porous plate and the inline sensors, aliquots of the effluent solutions were acidified with ultra high-purity concentrated $HNO_3$ and analyzed with ICP-MS and ICP-OES methods.

*2.8 Normalized concentration and quantification of the elemental release rates*

The normalized concentration ($NC_i$) was calculated from the element concentrations in the effluent solutions with Eqn. (3)

$$NC_i = \frac{\left(c_{i,L} - \bar{c}_{i,b}\right)}{f_i} \tag{3}$$

where $c_i$ is the effluent and average background solution concentration of element $i$ (mg/L) and $f_i$ is the mass fraction of element $i$ in the FBSR NAS waste form (unitless).

The results of chemical analyses on collected effluent samples are used to calculate a normalized release rate according to Pierce et al. (2006) and McGrail et al. (1996a)

$$r_i = \frac{4\phi q(c_{i,L} - c_{i,b})}{\rho S(1-\phi)\pi d^2 L f_i} \tag{4}$$

where $r_i$ is the normalized dissolution (release) rate of the $i$th element [g/(m$^2$ d)], $c_{i,L}$ is the effluent concentration of the $i$th element (g/m$^3$), $c_{i,b}$ is the background concentration of the $i$th element (g/m$^3$), $d$ is the column diameter (m), $L$ is the column length (m), $q$ is the volumetric flow rate (m$^3$/d), $S$ is the specific surface area of the granular FBSR NAS waste form sample (m$^2$/g), $\phi$ is the porosity (unitless), $\rho$ is the granular FBSR NAS waste form density (g/m$^3$), $f_i$ is the mass fraction of the *ith* element (unitless), and $\theta$ is the volumetric water content (unitless). The volumetric water content is calculated based on the mass of a volume of water in a fixed column volume, accounting for changes in the solution density resulting from temperature changes. The background concentration for most elements is typically below the estimated quantification limit (EQL) for the respective analysis. The EQL is defined as the lowest calibration standard that can be determined reproducibly during an analytical run within 10% of the certified value multiplied by the sample dilution factor. In cases where the analyte is below the EQL, the background concentration of the element is set at the value of the EQL. An estimate of the 2▲experimental uncertainty for the elemental release rates from the FBSR material was determined with error propagation. For additional details on the error propagation equation for PUF experiments see Pierce et al. (2006).

## 3 Results

### *3.1 XRD characterization of the unreacted FBSR material*

Powder XRD measurements were performed on an aliquot of unreacted FBSR LAW mineralized product. The measured XRD pattern is shown in Fig. 2 along with several standard mineral powder diffraction files (PDF$^{TM}$). The major reflections shown are consistent with the ~70 to 75% nepheline [$NaAlSiO_4$, PDF #19-1176] and ~10 to 15% sodium aluminum silicate [$NaAlSiO_4$, PDF #52-1342] similar to low carnegieite ($NaAlSiO_4$) or a hydrated nepheline. Minor shifts in the peaks corresponding to the sodium aluminum silicate phase were observed, perhaps indicating a minor amount of chemical or structural difference compared with the phase represented in the PDF$^{TM}$ database. Lesser amounts of nosean [$Na_6(Al_6Si_6O_{24}(Na_2SO_4]$, PDF# 74-1736] and anion-bearing sodalite (ideally $Na_8[Al_6Si_6O_{24}](NaCl)_2$) which combined accounts for ~10 to 15%. The values provided are semi-quantitative and represent the relative magnitude of the different minerals and are based upon whole pattern fitting of the XRD spectrum. In other words, nepheline is the dominant mineral contained in the FBSR NAS granular product which also contains a significant fraction of sodium aluminum silicate (similar to low-carnegiete) and anion-bearing

sodalite/nosean. The XRD analyses were conducted on FBSR NAS product with the excess coal removed by heating the material to 525°C overnight in an oxidizing atmosphere prior to testing. The heating process removed 5.57 wt% for 1104/1123 and 3.27 wt% for 1125 of unreacted coal for the FBSR LAW bed product (1104/1123) and the filter fines (1125), respectively.

*3.2 Rhenium oxidation state in the unreacted FBSR material*

The Re $L_2$-edge XANES spectra of the four standards are shown in Fig. 3a. Each spectrum is dominated by a large white line which lies just below the actual adsorption edge in energy. This feature is due to the allowed transition of the Re 2p-electrons into the vacant 5d-orbitals. The overall intensity of this feature reflects the number of vacancies in the 5d-orbitals, so the area of the white line becomes progressively larger as one progresses from $ReO_2$ (7 vacancies) to $ReO_3$ (9 vacancies) to $KReO_4$ and $ReO_4^-$-sodalite (10 vacancies). The spectra also shift to higher energies as the formal oxidation increases, which is due to decreased screening of the Re 2p-electrons. In addition to these major differences, the XANES region just above the edge contains features due to extended X-ray absorption fine structure (EXAFS), especially those due to multiple scattering. The major changes are clearly seen in Fig. 3a as one moves from $ReO_2$ through the $ReO_4^-$ compounds. The smaller EXAFS contributions may be seen in the size and spacing of the features at energies that are above the white line. In particular, the EXAFS contributions result in slightly different spectra for $KReO_4$ versus $ReO_4^-$-sodalite because the Re environments is not identical in the two materials. Although both materials contain the tetrahedral $ReO_4^-$ anion, the Re-O bond distance in $ReO_4^-$-sodalite, 1.655 ±0.006 Å (Pierce et al., submitted) is considerably shorter than bond in $NaReO_4$ = 1.728 ±0.002 Å (Atzesdorfer and Range, 1995) and $KReO_4$ = 1.723 ±0.004 Å (Lock and Turner, 1975; Morrow, 1960). The results confirm that under these processing conditions the oxidation state of Re remains unchanged and suggest the reduced conditions used to destroy the nitrite and nitrate species contained in the LAW stream during the production process are not reducing enough to convert Re(VII) to Re(IV) species in the FBSR NAS matrix.

The results of the linear combination fitting the XANES spectrum of FSBR 1125 are provided Table 2 and shown in Fig. 3b and strongly support the postulate that the perrhenate anion is present in the sodalite cage rather than existing as a separate perrhenate salt. Of the four standard spectra, only two, those of $KReO_4$ and $ReO_4^-$-sodalite, had contributions greater than their standard deviations. The large uncertainties in the contributions of $KReO_4$ and $ReO_4^-$-sodalite are due to the similarities of the spectra and should not be taken as an indication that any Re oxidation state other than heptavalent contributes to the spectrum of FBSR 1125. One surprising result of the

XANES analysis is indicated by the p-values of the standard spectra. In the case of $KReO_4$, the p-value of 0.390 means that the fit is not significantly improved by inclusion of this reference spectrum (Table 2). On the other hand, the p-value of 0.018 for $ReO_4^-$-sodalite indicates that the fit is significantly improved by its inclusion (Table 2). Qualitatively, this difference can also be seen in the similarity of the XANES spectrum of FBSR 1125 to that of $ReO_4^-$-sodalite, especially in the region of the small peak just above the white line in energy. In the XANES spectrum of $KReO_4$, this peak has greater intensity and occurs at lower energy than in the spectra of $ReO_4^-$-sodalite and FBSR 1125. Similar results were obtained for the FBSR 1123 sample. The Re release results discussed below are also consistent with the Re partitioning to a mineral phase rather than the water soluble perrhenate salt, such as $NaReO_4$ or $KReO_4$.

### *3.3 Computer monitored test metrics*

Results from the computer-monitored test metrics, volumetric water content (❑), pH, and electrical conductivity (✳), are shown in Fig. 4, 5, and 6. The sensor data were smoothed using a bi-square weighting, method where the smoothed data point, $y_s$, is given by $y_s$ [illegible] . The parameter [illegible] is a weighting coefficient calculated from a window surrounding the smoothing location in the set of the independent variables. A low-order polynomial regression (order 2 in this case) is used to compute [illegible] for each smoothed value. The smoothed data are provided as lines and were used to make qualitative assessments of the results shown in Fig. 4, 5, and 6.

Results shown in Fig. 4 illustrate that the average volumetric water content (❑) gradually increases with increasing reaction time from 0.32 ±0.03 for first 200 days to 0.56 ±0.02 for the final 200 days of testing. The observed episodic increases in the ❑, as shown in Fig. 4, is the result of the effluent line becoming plugged with colloidal reaction products (illustrated by vertical lines). These excursions were excluded from the average volumetric water content calculations. Attempts to collect and analyze this material were unsuccessful. Previous experiments with SCT02-98 material by McGrail et al. (2003a) also observed plugging of the porous plate. The results of SEM-EDS analysis of the porous plate from these early PUF experiments suggested that a Pb mineral phase was precipitating on the surface of the porous plate. Similarly to the volumetric water content, the effluent solution pH and electrical conductivity decreased as the testing time increased (Fig. 5 and Fig. 6).

*3.4 Effluent Solution chemistry*

Results from the analyses of effluent samples are provided in Fig. 7. Release of elements from the column illustrates a general trend of decreasing concentration with increasing reaction time. The normalized concentrations of Na, P, Re, and S are as much as $1 \times 10^2$ times greater than Al and $1 \times 10^4$ times greater than Si (Fig. 7). It is important to note that majority of the solution samples analyzed for the concentration of Ca, Cr, Fe, K, Mg, Mn, Pb, and Ti were below the EQL. The results for these elements were not included in Fig. 7.

The normalized concentration ($NC_i$) was calculated from the element concentrations in the effluent solutions with Eqn. (3). The results shown in Fig. 7 suggests that under these conditions Na-, P-, Re-, and S-bearing solid/mineral phase(s) are more soluble than Al- and Si-bearing solid/mineral phase(s). Although all the solutions exiting the PUF column were visibly clear, it is possible that colloids smaller than the 0.2-Om average pore diameter of the porous plate may be exiting the PUF column. Therefore, everything <0.2-Om was analyzed as being in solution. Movement and transport of colloids is to be expected because transport within a PUF column is typically advection-dominated. This can be demonstrated by calculating a Peclet ($P_e$) number for this experiment with Eqn. (5);

$$P_e = \frac{\left(\frac{q}{\theta A}\right) x}{D}, \qquad P_e \geq 4 \text{ (advection-dominated system)} \tag{5}$$

where $q$ is the flow rate ($2.3 \times 10^{-11}$ m$^3$/s), $\theta$ is the average volumetric water content (0.246), $A$ is the column area ($2.85 \times 10^{-4}$ m$^2$), $x$ is the column distance (0.0762 m), and $D$ is the molecular diffusion coefficient for water (assumed to be $1.0 \times 10^{-9}$ m$^2$/s). This calculation resulted in an average $P_e$ number of 25.2. This value clearly shows that this PUF test is advection dominated.

*3.5 Element release rate and mineral dissolution rate*

A comparison of the element release rates for the major components in the FBSR NAS granular product is shown in Fig. 8. Similar to the concentration data the rate of element release decreases as the reaction time increases. The results in Fig. 8 also illustrate that the steady-state release rates (estimated to occur after 200-days of reaction) for Al [$(4.8 \pm 0.6)\times10^{-5}$ g/(m$^2$ d)] and Si [$(2.7 \pm 0.5)\times10^{-5}$ g/(m$^2$ d)] is equivalent and Na [$(1.1 \pm 0.2)\times10^{-4}$ g/(m$^2$ d)] release is ~2 to 4 times faster than Al and Si, respectively. In comparison to Al and Si, the steady-state release rate for Re [$(5.7 \pm 0.9) \times 10^{-4}$ g/(m$^2$ d)] release is 10 to 20 times greater and S [$(2.0 \pm 0.4) \times 10^{-4}$ g/(m$^2$ d)] release is 4 to 7 times greater. Although the average steady-state Re release rate is ~2.8 times greater than the S

release rate, the similarity in the observed time-dependent release behavior suggests that perrhenate sodalite and nosean may be associated with one another. The slightly faster reaction rate for the perrhenate sodalite may be related to the possibility that Re may be present in the FBSR NAS product as a mixed salt anion-sodalite (Trill, 2002; Trill et al., 2002; Trill et al., 2003); in other words an anion-sodalite that contains multiple guest anions in the cage. There is a high probability for the formation of a mixed anion sodalite because other anions (i.e., Cl, $F^-$, $SO_4^{2-}$, etc.) are present in the FBSR feed material, specifically the LAW simulant, at concentrations that are several orders of magnitude greater than $ReO_4^-$. Although we suspect that the perrhenate sodalite contained in the FBSR NAS granular product is most-likely present as a mixed phased anion-sodalite—which has implications on the minerals stability and reactivity—measurements are being performed with the individual pure minerals (e.g., nosean and Cl-I-, and Re-bearing sodalites) for comparison to the FBSR NAS granular product results presented here [see Pierce et al. (submitted)].

*3.6 Characterization of reacted FBSR grains*

Analysis of reacted grains at various depths with powder XRD (Fig. 9) confirmed that samples removed from the top of the column had the most extensive alteration. In comparison to the unreacted sample (see Fig. 2), Fig. 9 suggests that the most reacted samples—which were taken from the 3.5-mm and 7.5-mm depth—have been significantly depleted in the $NaAlSiO_4$ phase that is similar to low carnegieite relative to the other phases present. The fractional change as a function of depth is illustrated in Fig. 10a and b and indicates the reaction front has progressed ~30-mm (i.e., halfway) into the column. The fraction of anion-sodalite and nosean has been depeleted in the upper most samples (e.g., 3.5-mm and 7.5-mm) with the distribution of minerals contained in the remaining samples staying relatively constant (Fig. 10a). A similar trend is shown for nepheline in Fig. 10b with the increase being largely associated with the depletion of a phase that resembles low carnegiete and the conversion of sodalite and nosean to nepheline. The observed depth dependent XRD profile occurs because of the constant leaching of elements at the column inlet which is caused by the addition of fresh DIW that dilutes the equilibrated pore-water and provides the chemical potential needed for additional leaching of the FBSR NAS matrix. Additionally, the order of reactivity for each mineral phase also plays a role in the observed XRD profile because the thermodynamic stability of each mineral is different. Thermodynamic measurements indicate the order of reactivity is nepheline > nosean > Cl-sodalite > Re-sodalite. Although the XRD results are semi-quantitative, they suggest that the mineral phase that resembles low carnegieite dissolves first and is the least durable of all the mineral phases contained in the

multiphase FBSR NAS waste form. The XRD results also indicate that the mineral distribution evolves with time but the dominant mineral phases contained in the FBSR NAS matrix are still present even after 2.5-years of leaching at 90°C and a high surface area-to-volume ratio.

## 4 Discussion

### *4.1 Mechanisms Controlling Al, Na, and Si Release*

Although the reaction mechanism for silicate weathering is still being debated, the generally accepted concept that describes silicate weathering is the leaching mechanism (Blum and Stillings, 1995; Nugent et al., 1998; Oelkers, 2001; Oelkers et al., 1994). The silicate leaching mechanism concept proceeds via a set of coupled processes that include **(1)** the selective removal of charge compensating cations (i.e., ion exchange of $H^+$ or $H_3O^+$ contained in bulk solution for cations in the mineral) and **(2)** protonation and rupture of Si—O—Si and Si—O—Al bonds (i.e., network hydrolysis) [see Oelkers et al. (2009), Schott (2009), and the references contained therein]. Under near-saturated conditions the aforementioned reaction mechanisms typically lead to the development of a hydrated surface layer that is depleted in aluminum as well as alkali and alkaline-earth metals and ranges in thickness from 20 to 1000 Å. It has been postulated that reconstruction of the silica network, which creates a silica-rich surface layer, can occur via molecular-scale reorganization either by repolymerization of silanol groups (Casey and Bunker, 1990; Casey et al., 1988), restructuring of the silica network (Tsomaia et al., 2003), and/or readsorption of silica (Banfield et al., 1995) at the mineral-solution interface. Hellman (2003; 2012) has questioned the process of surface reconstruction in the formation of surface layers by studying the interface between experimentally altered and non-altered feldspar using high resolution transmission electron microscopy. Hellman et al. (2003; 2012) concluded that the interface was chemically and structurally sharp on an atomic scale, and did not show the compositional profiles that would be expected from a solid state interdiffusion mechanism. They concluded that the data were better explained by an interfacial dissolution-reprecipitation mechanism, in which the dissolution reaction is initially stoichiometric, but is coupled with the precipitation of amorphous silica from a supersaturated boundary layer of fluid (i.e., a solution film in contact with the mineral surface that has a composition that is different than the bulk fluid).

In an attempt to gain additional insight into mechanisms controlling Al, Na, and Si release from the FBSR NAS matrix geochemical modeling with PHREEQC was used to qualitatively evaluate the possibility of solubility limited release. Three simulations were conducted and compared to the measured Al, Na, and Si steady-state effluent

concentrations (i.e., concentration after the first 200 days of testing). The model simulations consisted of estimating the Al, Na, and Si concentration based on the nepheline solubility and Si concentration based on amorphous $SiO_2$ and chalcedony solubility. The results shown in Fig. 11 suggest nepheline or the phase that resembles low carnegiete solubility is controlling the concentration of steady-state concentration of Al, whereas Na release is controlled by a combination of ion exchange and nepheline or the phase that resembles low carnegiete solubility, evident by the 2.3 to 3.7 higher release rate in comparison to Al. The deviation between the measured and predicted Si concentrations with respect to nepheline solubility (Fig. 11), suggest that Si release is being controlled by the formation of another phase; probably a Si-rich phase similar to amorphous silica or chalcedony (Fig. 12). The correlation between the measured Si concentrations to amorphous silica and chalcedony solubility suggests a hydrated surface layer may have formed on surface of altered FBSR grains. The inability to positively identify this phase in XRD and SEM analysis of reacted grains suggests the phase is amorphous and represents a minor component of the bulk sample, such as a surface coating on reacted grains.

Although the results presented cannot distinguish between the two mechanisms currently being debated (i.e., reconstruction versus dissolution-reprecipitation) within the geochemical community, the time-dependent evolution of the solution chemistry suggests the following steps are occurring: (1) the ion exchange as evident by the average Na ($7.9\times10^2$ g/m$^2$) normalized release being 2.3 and 3.7 times greater than Al ($3.4\times10^2$ g/m$^2$) and Si ($2.2\times10^2$ g/m$^2$) normalized release, respectively; (2) the dissolution of the silicate matrix, specifically the phase that resembles low carneigeite, evident by the depth dependent alteration phase evolution; and (3) the formation of a silica-rich surface layer evident by the dissolved Si concentration being at or near the solubility of amorphous $SiO_2$ or chalcedony. The formation of a Si-rich surface layer indicates that the alteration mechanism controlling multiphase FBSR matrix weathering is similar to other silicate minerals.

### *4.2 Re and S Release Mechanism and Implications for Hanford LAW Immobilization*

In an attempt to gain additional insight into mechanisms controlling Re and S release from the FBSR NAS matrix geochemical modeling with PHREEQC was used to qualitatively evaluate the possibility of solubility limited release. Two simulations were conducted and compared to the measured Re and S steady-state effluent concentrations (i.e., concentration after the first 200 days of testing). The model simulations consisted of estimating the Re concentration based on the Re-sodalite solubility and S concentration based on the nosean solubility. The results shown in Fig. 13 suggest the S and Re concentrations are within an order of magnitude of the nosean and Re-

sodalite solubility, respectively. The order of magnitude difference between the observed and predicted concentration along with the similarity in Re and S release provides additional indication for the proposed concept that the anion-sodalites contained in the FBSR NAS matrix are not pure and are present as mixed-anion sodalite phases.

The multiphase FBSR NAS ceramic waste form (which is composed of nepheline, low carneigiete, nosean, and sodalite) was evaluated as a potential host material for Hanford LAW. These results illustrate that rhenium in the FBSR NAS matrix is in the Re(VII) oxidation state, present as $NaReO_4$, and incorporated into the sodalite structure [probably as mixed anion-sodalite type structure $Na_8(Al_6Si_6O_{24})(SO_4)$ and $Na_8(Al_6Si_6O_{24})(ReO_4)_2$]. These results provide some credibility to the proposed concept that Tc(VII), similar to Re(VII), can be incorporated into the sodalite structure while in the presence of the other anions contained in the LAW waste stream at significantly higher concentrations. Although it has been demonstrated that the redox chemistry for Re and $^{99}Tc$ is significantly different (Lukens et al., 2007), the similarities in the atomic radii [1.373 Å for Re(VII) and 1.358 Å for Tc(VII)], as well as the ionic radii for Re(VII) and Tc(VII) at 0.56 Å, allows the perrhenate anion to serve as a close chemical analogue for the pertechnetate anion under oxidizing conditions (Icenhower et al., 2010). A comparison of the results discussed in this study to data previously collected on LAW glass (Fig. 14), indicates that Re release from the multiphase FBSR NAS granular product is an order of magnitude lower than $^{99}Tc$ release [$(2.1 \pm 0.3)\times10^{-2}$ g/(m$^2$ d)] from LAW glass (LAW AN102) (Pierce et al., 2006) when normalizing the rates using the BET surface area [$(6.1 \pm 0.9)\times10^{-4}$ g/(m$^2$ d)] and ~6 times faster (e.g., comparable) when using the geometric surface area [$(1.32 \pm 0.02)\times10^{-1}$ g/(m$^2$ d)]. Although glass represents the primary treatment option for Hanford LAW, these results suggests the multiphase FBSR NAS ceramic waste form may be a viable alternative technology for providing the supplemental treatment capacity required to meet the scheduled goals for Hanford cleanup.

## 5 Acknowledgements

This research was supported by the U.S. Department of Energy's (DOE) Environmental Management (EM) Tank Waste Management program and DOE EMs Office of River Protection, Immobilization of Low-Activity Waste Program. Portions of this research was performed at Oak Ridge National Laboratory (ORNL), Pacific Northwest National Laboratory (PNNL), Lawrence Berkeley National Laboratory (LBNL), Savannah River National Laboratory (SRNL), and Brookhaven National Laboratory (BNL). ORNL is operated by UT-Battelle, LLC for DOE under Contract No. DE-AC05-00OR22725. PNNL is operated by Battelle for DOE under Contract No. DE-AC05-76RL0-1830. LBNL is managed by the University of California for DOE under Contract No. DE-AC02-05CH11231. SRNL is managed by Savannah River Nuclear Solutions for DOE. A portion of this research was carried out with the use of the National Synchrotron Light Source an Office of Science, Office of Basic Energy Sciences, User Facility operated by BNL for DOE under Contract No. DE-AC02-98CH10886. Portions of this research were carried out at

the Stanford Synchrotron Radiation Lightsource, a Directorate of SLAC National Accelerator Laboratory and an Office of Science User Facility operated for DOE Office of Science by Stanford University. The SSRL Structural Molecular Biology Program is supported by the DOE Office of Biological and Environmental Research, and by the National Institutes of Health, National Center for Research Resources, Biomedical Technology Program (P41RR001209).

10

## 6 References


ASTM, 2008. Standard Practice for Prediction of the Long-Term Behavior of Waste Package Materials Including Waste Forms Used in Geologic Disposal of High-Level Nuclear Waste. American Society for Testing Material, West Conshohocken, Pennsylvania.

Atzesdorfer, A., Range, K.J., 1995. SODIUM METAPERRHENATE, NAREO4 - HIGH-PRESSURE SYNTHESIS OF SINGLE-CRYSTALS AND STRUCTURE REFINEMENT. Zeitschrift Fur Naturforschung Section B-a Journal of Chemical Sciences, 50(9): 1417-1418.

Banfield, J., Ferruzi, G., Casey, W.H., Westrich, H., 1995. HRTEM Study Comparing Naturally and Experimentally Weathered Pyroxenoids. Geochimica Cosmochimica Acta, 59: 19-31.

Barney, G., 1974. Fixation of Radioactive Wastes by Hydrothermal Reactions with Clays. Atlantic Richfield Hanford Company, Richland, WA.

Bickmore, B.R., Nagy, K.L., Young, J.S., Drexler, J.W., 2001. Nitrate-cancrinite precipitation on quartz sand in simulated Hanford tank solutions. Environmental Science & Technology, 35(22): 4481-4486.

Blum, A., Stillings, L. (Eds.), 1995. Feldspar dissolution kinetics. Chemical Weathering Rates of Silicate Minerals, 31. Mineralogical Society of America, Washington, DC, 291-351 pp.

Brantley, S., Mellot, N., 2000. Surface area and porosity of primary silicate minerals. American Mineralogist, 85: 1767-1783.

Brenchley, M.E., Weller, M.T., 1994. Synthesis and Structruer of $M_8[AlSiO_4]_6 (XO_4)_2$, M = Na, Li, K; X = Cl, Mn Sodalites. Zeolites, 14: 1994.

Brunauer, S., Emmet, P., Teller, E., 1938. Adsorption of gases in multimolecular layers. Journal of American Chemical Society, 60: 309-319.

Buhl, J.-C., Gesing, T.M., Gurris, C., 2001. Synthesis and crystal structure of rhodanide-enclathrated sodalite $Na_8[AlSiO_4]_6(SCN)_2$. Microporous and Mesoporous Materials, 50: 25-32.

Buhl, J.C., Englehardt, G., Felsche, J., 1989. Synthesis, X-ray Diffraction, and MAS NMR Characteristics of Tetrahydroxoborate Sodalite. Zeolites, 9: 40-44.

Campbell, B. et al., 2000. The cation-vacancy ordering transition in dehydrated $Na_6$ sodalite. Journal of Chemical Physics, 113(22): 10226-10239.

Casey, W.H., Bunker, B.C., 1990. Leaching of Mineral and Glass Surfaces During Dissolution. In: Hochella, M.F., Jr., White, A.F. (Eds.), Mineral-Water Interface Geochemistry. Mineralogical Society of America, Washington, D.C., pp. 397-426.

Casey, W.H., Westrich, H., Arnold, G., 1988. Surface chemistry of labradorite feldspar reacted with aqueous solutions at pH = 2, 3, and 12. Geochimica Cosmochimica Acta, 52: 2795-2807.

Caurant, D. et al., 2009. Glasses, Glass-Ceramics, and Ceramics for Immobilization of Highly Radioactive Nuclear Waste. Nova Science Publishers, Inc., New York.

Chorover, J. et al., 2003. Linking cesium and strontium uptake to kaolinite weathering in simulated tank waste leachate. Environmental Science & Technology, 37(10): 2200-2208.

Clinard, F., Peterson, D., Rohr, D., Hobbs, L., 1984a. Self-irradiation effects in $^{238}$Pu-substituted zirconolite: I. Temperature dependence of damage. Journal of Nuclear Materials, 126: 245-254.

Clinard, F., Rohr, D., Roof, R., 1984b. Structural damage in self-irradiated zirconolite-based ceramic. Nuclear Instruments and Methods in Physics Research B, 1: 581-586.

Deer, W., Howie, R., Zussman, J., 1963. Rock-Forming Minerals, Vol. IV. John Wiley & Sons, Inc, New York, NY.

Deng, Y.J., Flury, M., Harsh, J.B., Felmy, A.R., Qafoku, O., 2006a. Cancrinite and sodalite formation in the presence of cesium, potassium, magnesium, calcium and strontium in Hanford tank waste simulants. Applied Geochemistry, 21(12): 2049-2063.

Deng, Y.J., Harsh, J.B., Flury, M., Young, J.S., Boyle, J.S., 2006b. Mineral formation during simulated leaks of Hanford waste tanks. Applied Geochemistry, 21(8): 1392-1409.

DOE, 2012. Final Tank Closure and Waste Management Environmental Impact Statement for the Hanford Site. DOE/EIS-0391, US Department of Energy, Office of River Protection, Richland, Washington.

Downward, L., Booth, C., Lukens, W., Bridges, F., 2007. A Variation of the F-Test for Determining Statistical Relevance of Particular Parameters in EXAFS Fits, AIP Conference. AIP Conference Proceedings. American Institute of Physics, pp. 129-131.

Fanning, T. et al., 2003. Status of Ceramic Waste Form Degradation and Radionuclide Release Modeling. ANL-03/8, Argonne National Laboratory, Argonne, IL.

Fechtelkord, M., 2000. Influence of Sodium Ion Dynamics on the $^{23}$Na Quadrupolar Interaction in Sodalite: A High-Temperature $^{23}$Na MAS NMR Study. Solid State Nuclear Magnetic Resonance, 18: 70-88.

Gesing, T.M., Buhl, J.C., 1998. Crystal structure of a carbonate-nosean Na-8 AlSiO4 (6)CO3. European Journal of Mineralogy, 10(1): 71-77.

Harker, A.B., 1988. Tailored ceramics. In: Lutze, W., Ewing, R. (Eds.), Radioactive Waste Forms for the Future. North-Holland, Amsterdam, pp. 335-392.

Hatch, L., 1953. Ultimate Disposal of Radioactive Waste. American Journal of Science, 41: 410-421.

Hellmann, R., Penisson, J., Hervig, R., Thomassin, J., Abrioux, M., 2003. A EFTEM/HRTEM high resolution study of the near surface of labradorite feldspar altered at acid pH: evidence for interfacial dissolution-reprecipitation. Physics and Chemistry of Minerals, 30: 192-197.

Hellmann, R. et al., 2012. Unifying natural and labortory chemical weathering with interfacial dissolution-reprecipitation: A study based on the nanometer-scale chemistry of fluid-silicate interfaces. Chemical Geology, 294-295: 203-216.

Hench, L.L. et al., 1981. The Evaluation and Selection of Candidate High Level Waste Forms, Report No.3, Springfield, VA.

Hench, L.L., Clark, D.E., Harker, A.B., 1986. Nuclear waste solids. Journal of Materials Science, 21: 1457-1478.

Icenhower, J.P., Qafoku, N.P., Zachara, J.M., Martin, W.J., 2010. THE BIOGEOCHEMISTRY OF TECHNETIUM: A REVIEW OF THE BEHAVIOR OF AN ARTIFICIAL ELEMENT IN THE NATURAL ENVIRONMENT. American Journal of Science, 310(8): 721-752.

Icenhower, J.P. et al., 2006. Dissolution kinetics of pyrochlore ceramics for the disposition of plutonium. American Mineralogist, 91: 39-53.

Jantzen, C., 2002. Engineering study of the Hanford Low Activity Waste (LAW) steam reforming process. WSRC-TR-2002-00317, Savannaah River Technology Center, Aiken, SC.

Jantzen, C., Marra, J., Pariezs, J., 2004. Analysis of raw materials for fluidized bed steam reforming. SRNL-ITB-2004-004, Savannah River National Laboratory, Aiken, SC.

Johnson, G.M., Mead, P.J., Weller, M.T., 2000. Synthesis of a range of anion-containing gallium and germanium sodalites. Microporous and Mesoporous Materials, 38: 445-460.

Lee, W., Ojovan, M., Stennett, M., Hyatt, N., 2006. Immobilization of Radioactive Waste in Glasses, Glass Composite Materials, and Ceramics. Advances in Applied Ceramics, 105(1): 3-12.

Lock, C., Turner, G., 1975. A Reinvestigation of the Crystal Structure of Potassium Perrhenate. Acta Crystallographica Section B: Structural Crystallography and Crystal Chemistry, 31(6): 1764-1765.

Lorier, T., Pareizs, J., Jantzen, C.M., 2005. Single Pass Flow Through (SPFT) Testing of Fluidized Bed Steam Reforming (FBSR) Waste Forms, Westinghouse Savannah River Company, Aiken, SC.

Lukens, W. et al., 2007. Dissimilar behavior of technetium and rhenium in borosilicate waste glass as determined by X-ray absorption spectroscopy. Chemical Materials, 19(3): 559-566.

Lumpkin, G., 2006. Ceramic Waste Forms for Actinides. Elements, 2: 365-372.

Lutze, W., Ewing, R., 1988. Radioactive Waste Forms for the Future. North Holland, Amsterdam.

Mahoney, L., Rassat, S., 2003. Tank 241-S-109 Cold Saltcake Simulant Formulation, Pacific Northwest National Laboratory, Richland, WA.

Mann, F.M., Puigh, R.J., Khaleel, R., Finfrock, S., McGrail, B.P., Bacon, D.H., Serne, R.J., 2003. Risk Assessment Supporting the Decision on the Initial Selection of Supplemental ILAW Technologies. RPP-17675, Pacific Northwest national Laboratory, Hanford, WA.

Mashal, K., Harsh, J.B., Flury, M., Felmy, A.R., Zhao, H.T., 2004. Colloid formation in Hanford sediments reacted with simulated tank \waste. Environmental Science & Technology, 38(21): 5750-5756.

Mattigod, S.V. et al., 2006. Synthesis and structure of perrhenate sodalite. Microporous and Mesoporous Materials, 91(1-3): 139-144.

McGrail, B., Ebert, W., Bakel, A., Peeler, D., 1997. Measurement of kinetic rate law parameters on a Na-Ca-Al borosilicate glass for low-activity waste. Journal of Nuclear Materials, 249: 175-189.

McGrail, B. et al., 2003a. Initial Suitability Evaluation of Steam-Reformed Low Activity Waste for Direct Land Disposal. PNWD-3288/WTP-RPT-097, Rev. 0, Battelle, Pacific Northwest Division, Richland, WA.

McGrail, B.P., Lindenmeier, C., Martin, P.F., Gee, G., 1996a. The Pressurized Unsaturated Flow (PUF) Test: A New Method for Engineered-Barrier Materials Evaluation. In: Jain, V., Peeler, D.K. (Editors), Environmental Issues and Waste Management Technologies in the Ceramic and Nuclear Industries II. American Ceramic Society, Westerville, Ohio, pp. 317-329.

McGrail, B.P., Lindenmeier, C.W., Martin, P.F., 1999. Characterization of Pore Structure and Hydraulic Property Alteration in Pressurized Unsaturated Flow Tests. In: Wronkiewicz, D.J., Lee, J.H. (Editors), Material Research Symposium Proceedings: Scientific Basis for Nuclear Waste Management. Material Research Society, Warrendale, PA, pp. 421-428.

McGrail, B.P., Lindenmeier, C.W., Martin, P.F., Gee, G.W., 1996b. The Pressurized Unsaturated Flow (PUF) Test: A New Method for Engineered-Barrier Materials Evaluation. In: Jain, V., Peeler, D.K. (Eds.), Environmental Issues and Waste Management Technologies in the Ceramic and Nuclear Industries II. The American Ceramic Society, Westerville, Ohio, pp. 317-329.

McGrail, B.P., Martin, P.F., Schaef, H.T., Lindenmeier, C.W., Owen, A.T., 2000. Glass/Ceramic Interactions In The Can-In-Canister Configuration For Disposal Of Excess Weapons Plutonium. In: Smith, R.W., Shoesmith, D.W. (Editors), Material Research Symposium Proceedings Scientific Basis for Nuclear Waste; Management XXIII. Material Research Society, pp. 345-352.

McGrail, B.P. et al., 2003b. Laboratory Testing of Bulk Vitrified and Steam Reformed Low-Activity Waste Forms to Support A Preliminary Risk Assessment for an Integrated Disposal Facility. PNNL-14414, Pacific Northwest National Laboratory, Richland, WA.

Mon, J., Deng, Y.J., Flury, M., Harsh, J.B., 2005. Cesium incorporation and diffusion in cancrinite, sodalite, zeolite, and allophane. Microporous and Mesoporous Materials, 86(1-3): 277-286.

Morrow, J., 1960. The crystal structure of $KReO_4$. Acta Crystallographica, 13: 443-445.

Moschetti, T. et al., 2000. Characterization of a Ceramic Waste Form Encapsulating Radioactive Electrorefiner Salt. In: Smith, R., Shoesmith, D. (Editors), Scientific Basis for Nuclear Waste Management XXIII. Material Research Society, Pittsburgh, PA, pp. 577-582.

NRC, 2011. Waste Forms Technology and Performance Final Report. The National Academies Press, Washington, DC.

Nugent, M., Brantley, S.L., Pantano, C.G., Maurice, P., 1998. The influence of natural mineral coatings on feldspar weathering. Nature, 395(6702): 588-591.

O'Holleran, T. et al., 1997. Glass-Ceramic Waste Forms for Immobilizing Plutonium. In: Gray, W., Triay, I. (Editors), Scientific Basis for Nuclear Waste Management XX. Material Research Society, pp. 1251-1258.

Oelkers, E.H., 2001. General kinetic description of multioxide silicate mineral and glass dissolution. Geochimica Et Cosmochimica Acta, 65(21): 3703-3719.

Oelkers, E.H., Schott, J. (Eds.), 2009. Thermodynamic and Kinetics of Water Rock Interactions. Reviews in Mineralogy and Geochemistry, 70. Mineralogical Society of Amercia, Chantilly, VA.

Oelkers, E.H., Schott, J., Devidal, J.L., 1994. The Effect of Aluminum, pH, and Chemical Affinity on the Rates of Aluminosilicate Dissolution Reactions. Geochimica et Cosmochimica Acta, 58(9): 2011-2024.

Olson, A., Soelberg, N., Marshall, D., Anderson, G., 2004. Fluidized Bed Steam Reforming of Hanford LAW Using THOR$^{SM}$ Mineralizing Technology. INEEL/EXT-04-02492, Idaho National Engineering and Environmental Laboratory, Idaho Falls, ID.

ORP, 2011. River Protection Project System Plan: Retrieve and Treat Hanford's Tank Waste and Close the Tank Farms to Protect the Columbia River. ORP-11242, Rev.6, US Department of Energy, Office of River Protection, Richland, Washington.

Parkhurst, D.L., Appelo, C.A.J., 1999. User's guide to PHREEQC (version 2): a computer program for speciation, batch-reaction, one-dimensional transport, and inverse geochemical calculations, U.S. Geological Survey, Denver, Colorado.

Pauling, L., 1930. The structure of sodalite and helvite. Zeitschrift fur Kristallographie, 74: 213.

Pierce, E.M., Bacon, D.H., 2011. Combined experimenal and computational approach to predict the glass-water reaction. Nuclear Technology, 176: 1-18.

Pierce, E.M., Lilova, K., Lukens, W., Navrotsky, A., Fitts, J., submitted. Perrhenate Sodalite: Structure, Thermodynamic Characterization, and Dissolution. Geochimica et Cosmochimica Acta.

Pierce, E.M. et al., 2005. Laboratory Testing of Bulk Vitrified Low-Activity Waste Forms to Support the 2005 Integrated Disposal Facility Performance Assessment. PNNL-15126, Pacific Northwest National Laboratory, Richland, WA.

Pierce, E.M. et al., 2007. Accelerated weathering of high-level and plutonium-bearing lanthanide borosilicate waste glasses under hydraulically unsaturated conditions. Applied Geochemistry, 22(9): 1841-1859.

Pierce, E.M. et al., 2004. Waste Form Release Data Package for the 2005 Integrated Disposal Facility Performance Assessment. PNNL-14805, Pacific Northwest National Laboratory, Richland, WA.

Pierce, E.M., McGrail, B.P., Valenta, M.M., Strachan, D.M., 2006. The Accelerated Weathering of a Radioactive Low-Activity Waste Glass Under Hydraulically Unsaturated Conditions: Experimental Results from a Pressurized Unsaturated Flow (PUF) Test. Nuclear Technology, 155(2): 133-148.

Pierce, E.M., Rodriguez, E.A., Calligan, L.J., Shaw, W.J., McGrail, B.P., 2008. An experimental study of the dissolution rates of simulated aluminoborosilicate waste glasses as a function of pH and temperature under dilute conditions. Applied Geochemistry, 23(9): 2559-2573.

Qafoku, N. et al., 2003a. Aluminum effect on dissolution and precipitation under hyperalkaline conditions: I. Liquid phase transformations. Journal of Environmental Quality, 32: 2354-2363.

Qafoku, N. et al., 2003b. Aluminum Effect on Dissolution and Precipitation under Hyperalkaline Conditions: II. Solid Phase Transformations. Journal of Environmental Quality, 32: 2364-2372.

Ravel, B., 2005. ATHENA and ARTEMIS interactie graphical data analysis using IFEFFIT. Physica Scripta, T115: 1007-1010.

Ringwood, A., Kesson, S., Ware, N., Hibberson, W., Major, A., 1978. Immobilization of High Level Nuclear Reactor Wastes in SYNROC. Nature, 278: 219-223.

Rivera, N. et al., 2011. Cesium and strontium incorporation into zeolite-type phases during homogeneous nucleation from caustic solutions. American Mineralogist, 96: 1809-1820.

Schott, J., Pokrovsky, O., Oelkers, E.H., 2009. The link between mineral dissolution/precipitation kinetics and solution chemistry. In: Oelkers, E.H., Schott, J. (Eds.), Thermodynamics and kinetics of water-rock

interaction. Reviews in Mineralogy & Geochemistry. Mineralogical Society of America, Chantilly, Virginia, pp. 207-253.

Serne, R.J., Zachara, J.M., Burke, D., 1998. Chemical information on tank supernatants, Cs adsorption from tank liquids onto Hanford sediments, and field observations of Cs migration from past tank leaks., Pacific Northwest National Laboratory, Richland, WA.

Shannon, S., Campbell, B., Metiu, H., Blake, N., 2000. Cation-vacancy ordering in dehydrated Na6[AlSiO4]6. Journal of Chemical Physics, 113(22): 10215-10225.

Sinkler, W., O'Holleran, T., Frank, S., Richmann, M., Johnson, S., 2000. Characterization of a Glass Bonded Ceramic Waste Form Loaded with U and Pu. In: Smith, R., Shoesmith, D. (Editors), Scientific Basis for Nuclear Waste Management XXIII. Material Research Society, Pittsburgh, PA, pp. 423-429.

Soelberg, N., Marshall, D., Taylor, D., Bates, S., 2004. Phase 2 TWR Steam Reforming Tests for Sodium-Bearing Waste Treatment. INEEL/EXT-04-010494, Idaho National Engineering and Environmental Laboratory, Idaho Falls, Idaho.

Srdanov, V.I., Harrison, W.T.A., Gier, T.E., Stucky, G.D., 1994. Structure and Spectroscopy of Sodalite Containing $MnO_4^-$ Ions. Journal of Physical Chemistry B, 98: 4673-4676.

Stefanovsky, S., Yudintsev, S., Giere, R., Lumpkin, G., 2004. Nuclear waste forms. In: Giere, R., Stille, P. (Eds.), Energy, Waste, and the Environment: A Geochemical Perspective. Geological Society of London Special Publication, pp. 36-63.

Trill, H., 2002. Sodalite Solid Solution System. Synthesis, Topotactic Transformations, and Investigation of Framewok-Guest and Guest-Guest Interactions., Westfalische Wilhelms Universitat, Munster.

Trill, H., Eckert, H., Srdanov, V., 2002. Topotactic Transformations of Sodalite Cages: Synthesis and NMR Study of Mixed Salt-Free and Salt-Bearing Sodalites. Journal of the American Chemical Society, 124: 8361-8370.

Trill, H., Eckert, H., Srdanov, V., 2003. Mixed Halide Sodalite Solid Solution System. Hydrothermal Synthesis and Structural Characterization by Solid State NMR. Journal of Physical Chemistry B, 107: 8779-8788.

Tsomaia, N., Brantley, S.L., Hamilton, J.P., Pantano, C.G., Mueller, K., 2003. NMR evidence for formation of octahedral and tetrahedral Al and repolymerization of the Si network during dissolution of aluminosilicate glass and crystal. American Mineralogist, 88: 54-67.

Weber, W., Wald, J., Matzke, H., 1986. Effects of self-radiation damage in Cm-doped $Gd2Ti_2O_7$ and $CaZrTi_2O_7$. Journal of Nuclear Materials, 138: 196-209.

Wierenga, P.J. et al., 1993. Soil Characterization Methods for Unsaturated Low-Level Waste Sites. PNL-8480, Pacific Northwest Laboratory, Richland, Washington.

Zachara, J.M. et al., 2007. Geochemical processes controlling migration of tank wastes in Hanford's vadose zone. Vadose Zone Journal, 6: 985-1003.

Zhao, H.T., Deng, Y.J., Harsh, J.B., Flury, M., Boyle, J.S., 2004. Alteration of kaolinite to cancrinite and sodalite by simulated hanford tank waste and its impact on cesium retention. Clays and Clay Minerals, 52(1): 1-13.

**Figures**

Fig. 1. Scanning Electron Microscopy image of 149 to 75 mm sized grains of the FBSR material as well as an image at increased magnification. The larger image illustrates that the larger grain is an aggregation of smaller particles....26

Fig. 2. Background subtracted bulk XRD spectra of FBSR granular material for two size fractions shown with the powder diffraction files for nepheline (PDF# 35-0424), nosean (PDF# 74-1736), sodium aluminum silicate phase (PDF# 52-1342), and quartz (PDF# 46-1045). ....27

Fig. 3. Re $L_2$-edge XANES spectra of the four standards used in fitting the XANES spectrum of the FBSR NAS granular product. Re $L_2$-edge XANES spectra of the FBSR NAS product and spectrum fit along with a comparison to $KReO_4$ and $ReO_4$-Sodalite. ....27

Fig. 4. Computer-monitored test metrics for the volumetric water content of the column. The grey lines are the bi-squared smoothed fit of the raw data and are provided as a guide to the eye. Vertical lines correspond to points when the effluent lines became plugged. ....28

Fig. 5. Computer-monitored test metrics for the pH of the effluent solution exiting the column. The grey lines are the bi-squared smoothed fit of the raw data and are provided as a guide to the eye. ....29

Fig. 6. Computer-monitored test metrics for the electrical conductivity of the effluent solution exiting the column. The grey lines are the bi-squared smoothed fit of the raw data and are provided as a guide to the eye. ....29

Fig. 7. Normalized concentration, in mg/L, as a function of time, in days, for Al, Na, and Si on the left (a) and P, Re, and S on the right (b). ....30

Fig. 8. Normalized dissolution rate, in g/($m^2$ d), as a function of time, in days, for Al, Na, and Si on the left (a) and P, Re, and S on the right (b). ....30

Fig. 9. X-ray Diffraction Pattern of the Reacted FBSR NAS Waste Form after 356-days in a PUF test at 90°C. ....31

Fig. 10. Relative Fraction of the Dominant Minerals as a Function of Depth for the Reacted NAS FBSR NAS Waste Form. The dashed line is the Average Fraction of the Dominant Minerals in the Unreacted FBSR NAS Waste Form. ....32

Fig. 11. Steady-State Effluent Concentration (mmol/L) of Al, Na, and Si Measured in the PUF experiment starting at day 200 as a function of the average pH. Solid line Represent the Calculated Solubility for Nepheline. ....32

Fig. 12. Steady-State Concentration (mmol/L) of Si Measured in the PUF Experiment Starting at Day 200 as a Function of the Average pH. Solid Black and Dark Gray lines Represents the Calculated Solubility for $SiO_2$ (am) and Chalcedony. ....33

Fig. 13. Steady-State Concentration (mmol/L) of S and Re Measured in the PUF Experiment Starting at Day 200 as a Function of the Average pH. Solid Black and Dark Gray lines Represents the Calculated Solubility for Nosean and Re-sodalite. ....34

Fig. 14. Comparison of the Element Release Rate for Re and S from FBSR NAS Waste Form and $^{99}Tc$ from LAW Glass AN102 from Pierce et al. (2006). Each Pressurized Unsaturated Flow Experiment was Performed Under the same Test Conditions (90°C and 2 mL/day). ....35

1

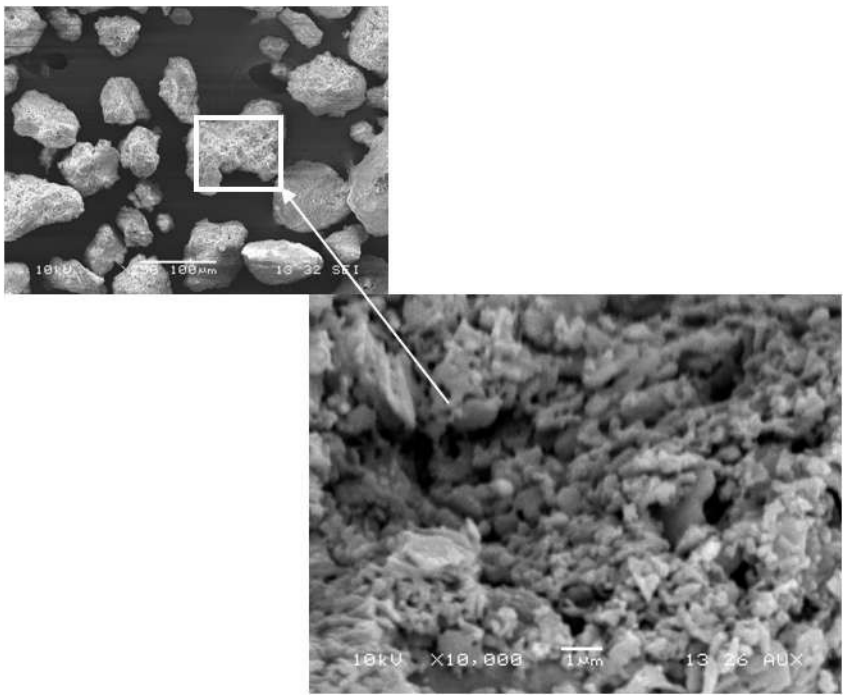


**Fig. 1.** Scanning Electron Microscopy image of 149 to 75 mm sized grains of the FBSR material as well as an image at increased magnification. The larger image illustrates that the larger grain is an aggregation of smaller particles.

1

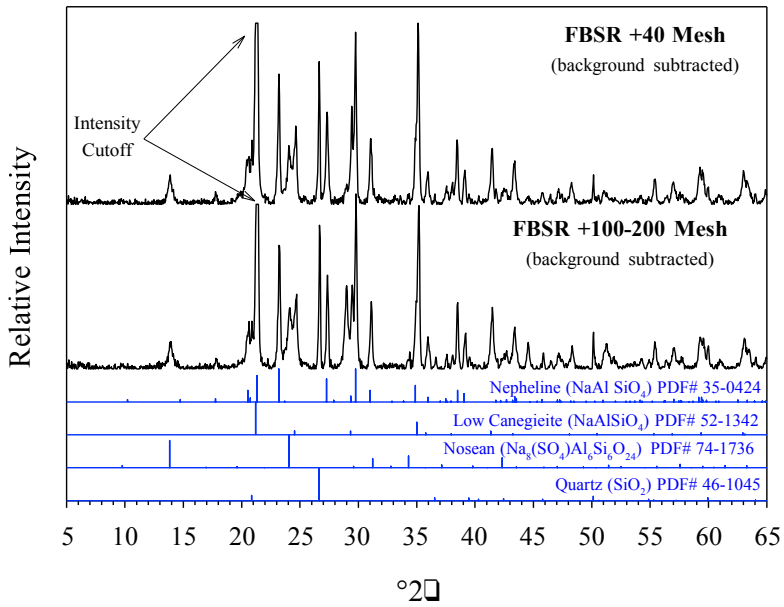


**Fig. 2.** Background subtracted bulk XRD spectra of FBSR granular material for two size fractions shown with the powder diffraction files for nepheline (PDF# 35-0424), nosean (PDF# 74-1736), sodium aluminum silicate phase (PDF# 52-1342), and quartz (PDF# 46-1045).

2

3

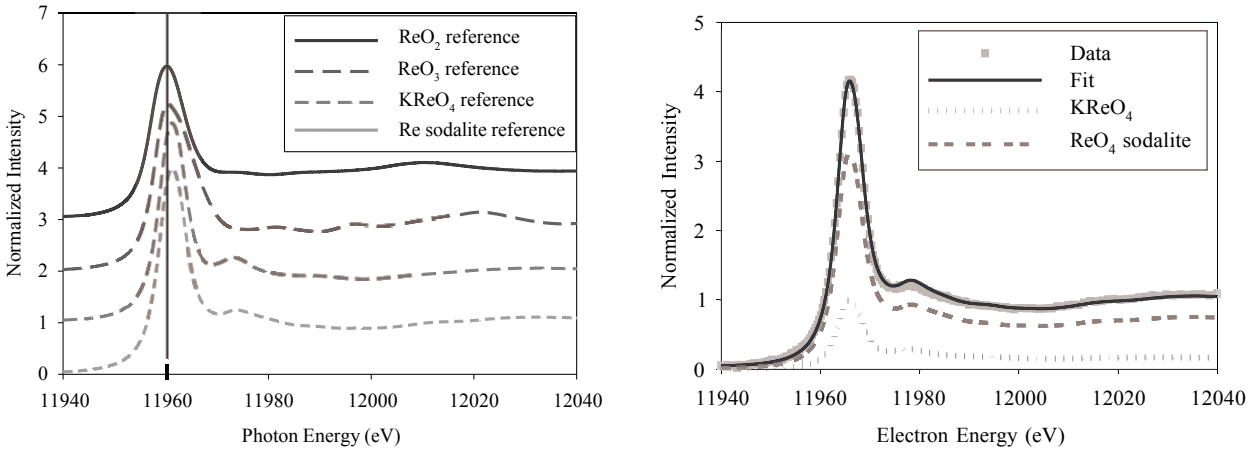


**Fig. 3.** Re $L_2$-edge XANES spectra of the four standards used in fitting the XANES spectrum of the FBSR NAS granular product. Re $L_2$-edge XANES spectra of the FBSR NAS product and spectrum fit along with a comparison to $KReO_4$ and $ReO_4$-Sodalite.

4

5

6

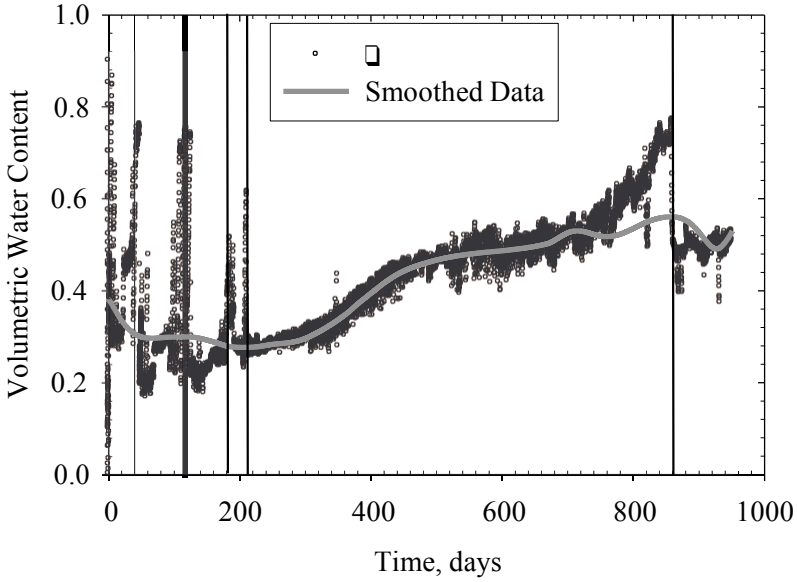


**Fig. 4.** Computer-monitored test metrics for the volumetric water content of the column. The grey lines are the bi-squared smoothed fit of the raw data and are provided as a guide to the eye. Vertical lines correspond to points when the effluent lines became plugged.

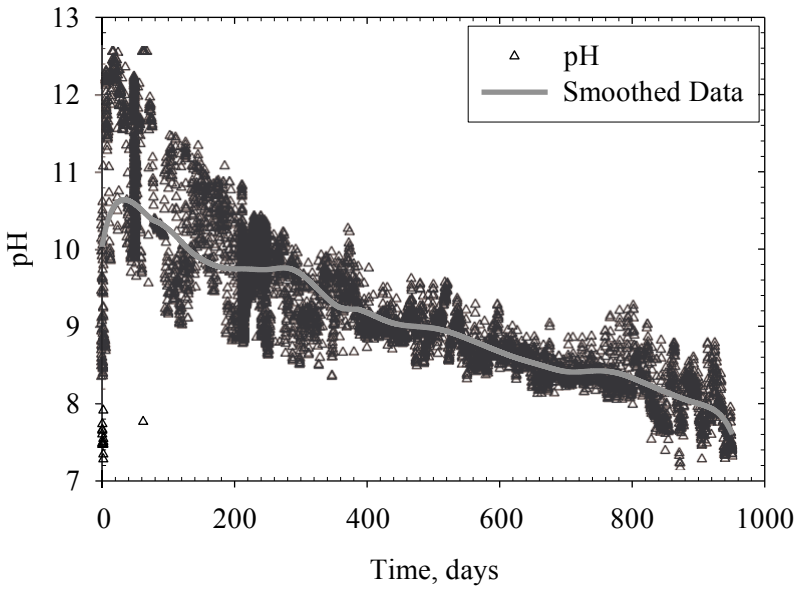


**Fig. 5.** Computer-monitored test metrics for the pH of the effluent solution exiting the column. The grey lines are the bi-squared smoothed fit of the raw data and are provided as a guide to the eye.

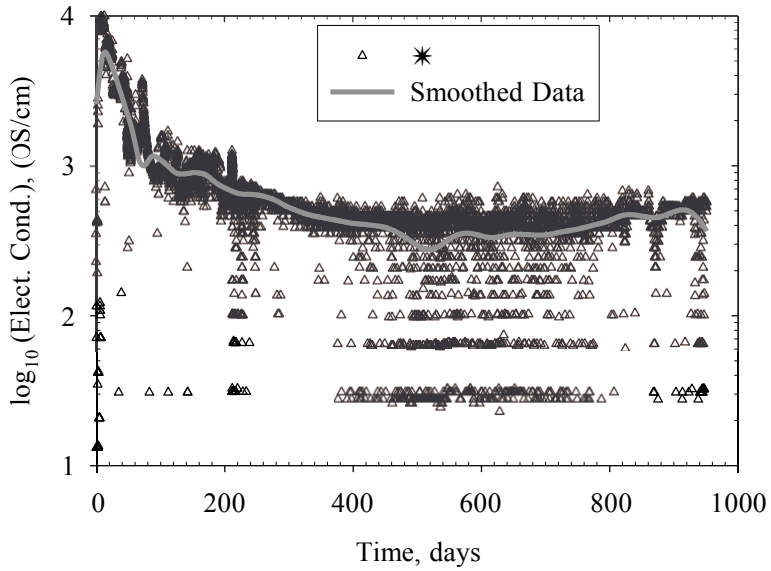


**Fig. 6.** Computer-monitored test metrics for the electrical conductivity of the effluent solution exiting the column. The grey lines are the bi-squared smoothed fit of the raw data and are provided as a guide to the eye.

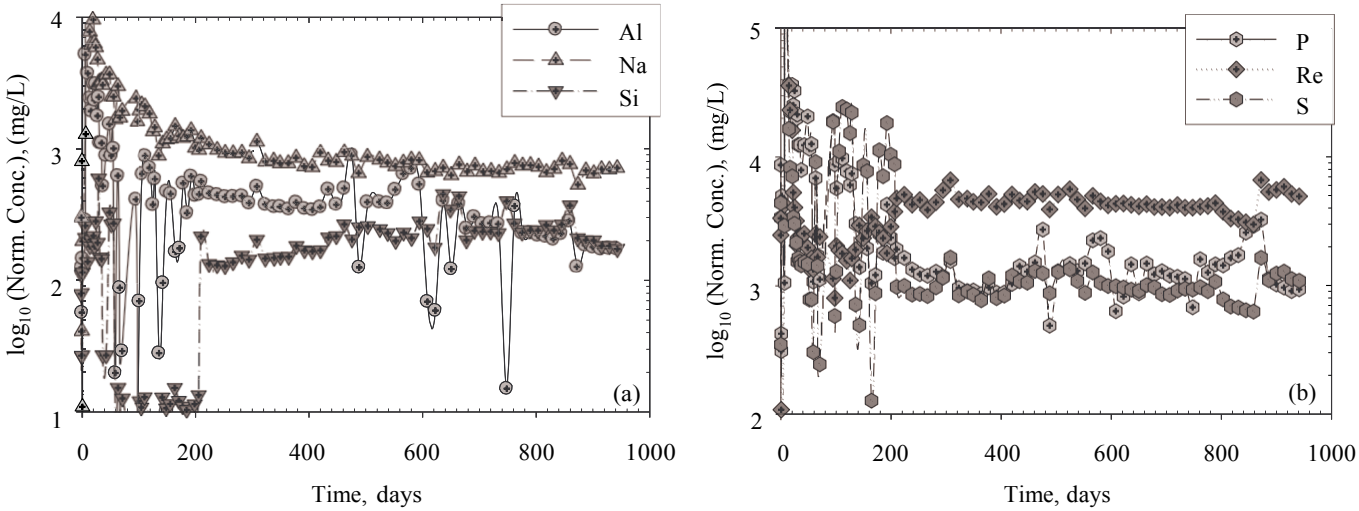


**Fig. 7.** Normalized concentration, in mg/L, as a function of time, in days, for Al, Na, and Si on the left (a) and P, Re, and S on the right (b).

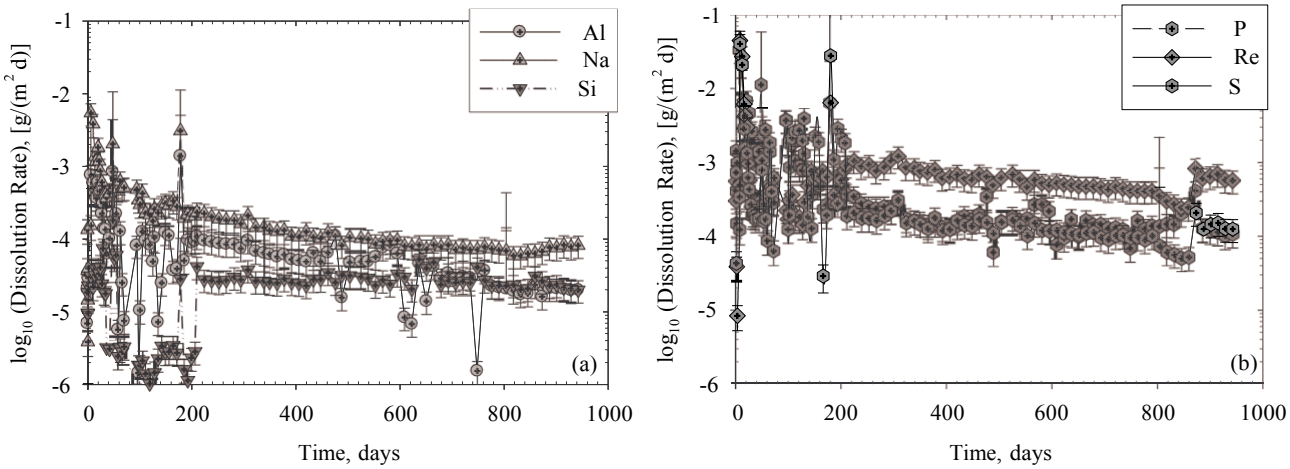


**Fig. 8.** Normalized dissolution rate, in g/(m$^2$ d), as a function of time, in days, for Al, Na, and Si on the left (a) and P, Re, and S on the right (b)

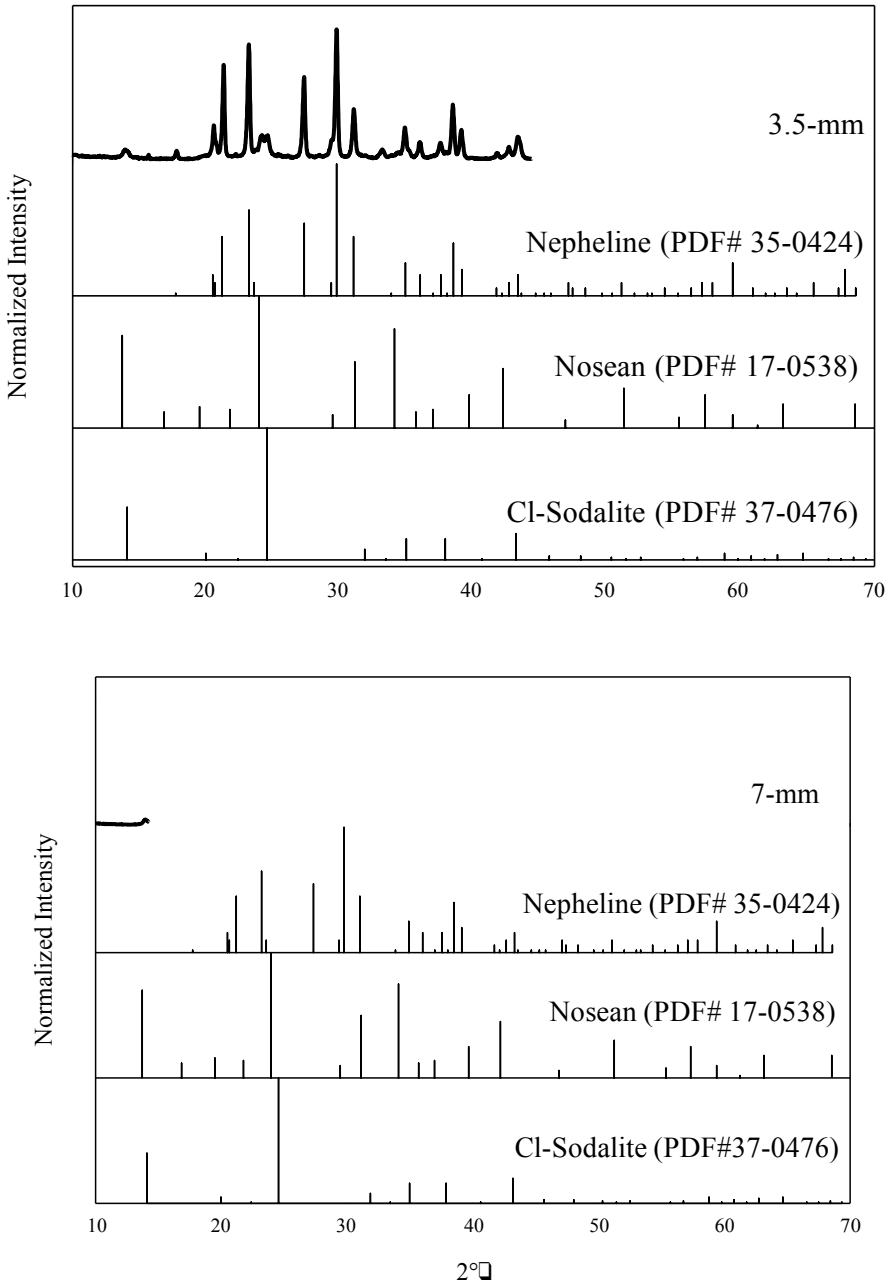


**Fig. 9.** X-ray Diffraction Pattern of the Reacted FBSR NAS Waste Form after 356-days in a PUF test at 90°C.

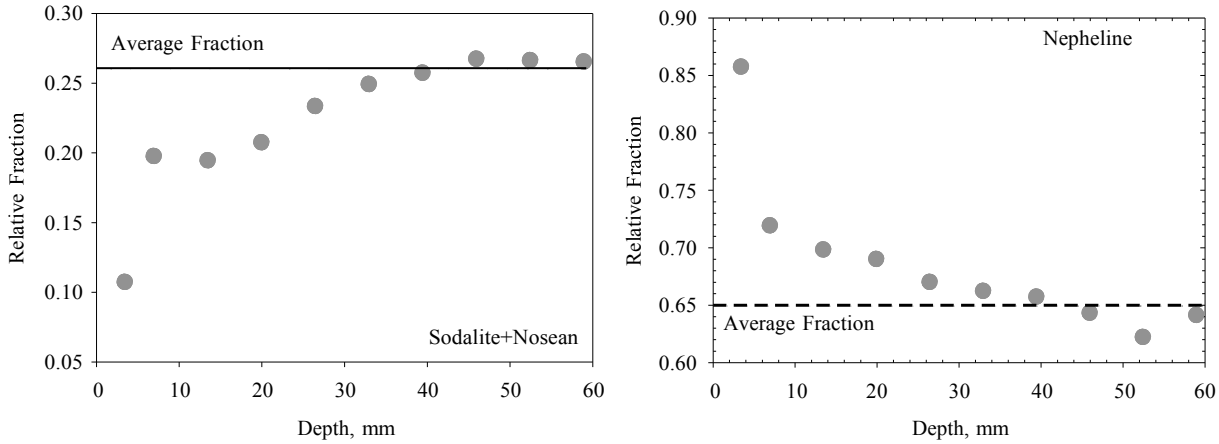


**Fig. 10.** Relative Fraction of the Dominant Minerals as a Function of Depth for the Reacted NAS FBSR NAS Waste Form. The dashed line is the Average Fraction of the Dominant Minerals in the Unreacted FBSR NAS Waste Form.

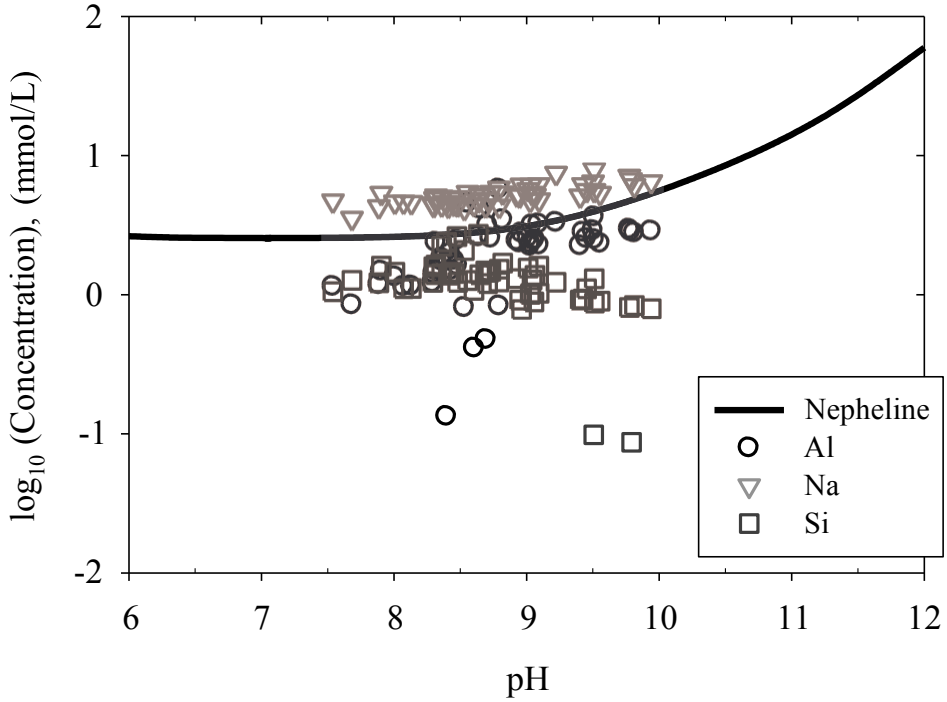


**Fig. 11.** Steady-State Effluent Concentration (mmol/L) of Al, Na, and Si Measured in the PUF experiment starting at day 200 as a function of the average pH. Solid line Represent the Calculated Solubility for Nepheline.

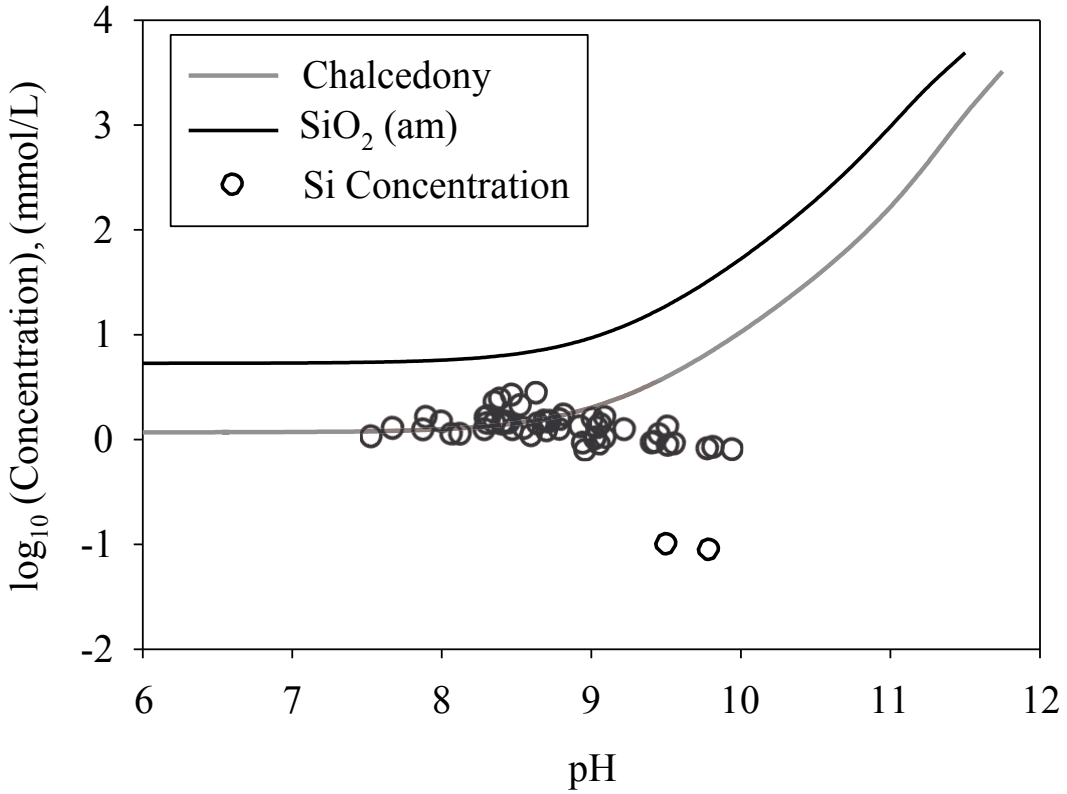


**Fig. 12.** Steady-State Concentration (mmol/L) of Si Measured in the PUF Experiment Starting at Day 200 as a Function of the Average pH. Solid Black and Dark Gray lines Represents the Calculated Solubility for $SiO_2$ (am) and Chalcedony.

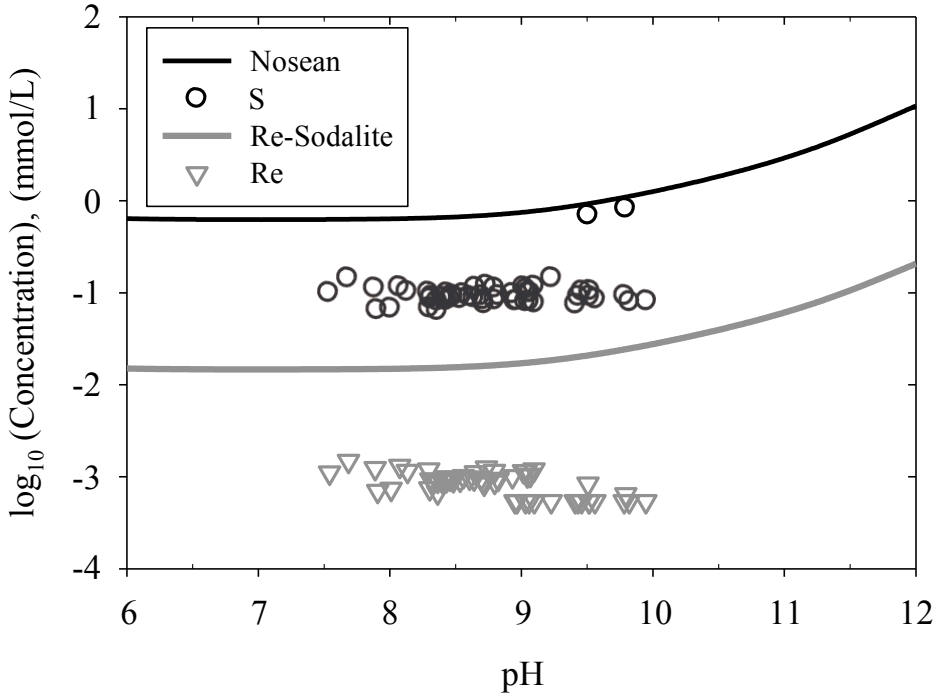


**Fig. 13.** Steady-State Concentration (mmol/L) of S and Re Measured in the PUF Experiment Starting at Day 200 as a Function of the Average pH. Solid Black and Dark Gray lines Represents the Calculated Solubility for Nosean and Re-sodalite.

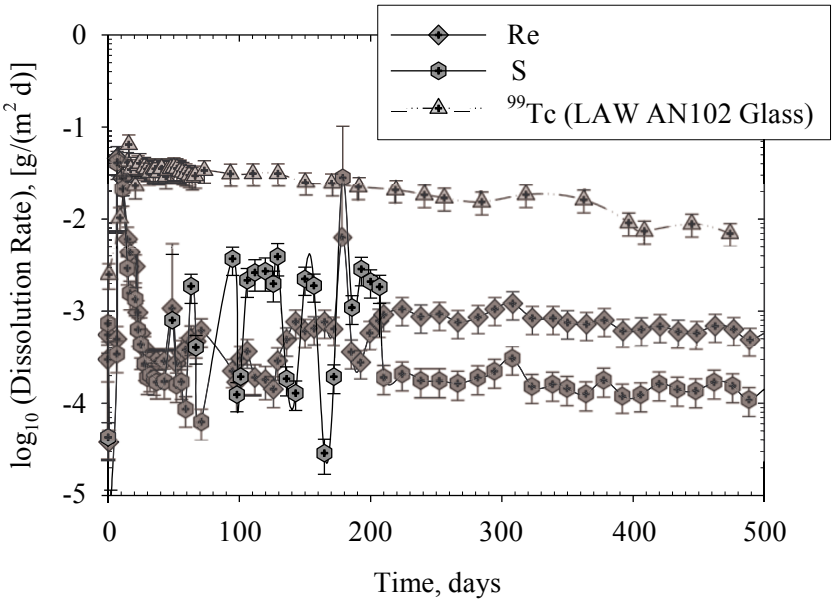


**Fig. 14.** Comparison of the Element Release Rate for Re and S from FBSR NAS Waste Form and $^{99}$Tc from LAW Glass AN102 from Pierce et al. (2006). Each Pressurized Unsaturated Flow Experiment was Performed Under the same Test Conditions (90°C and 2 mL/day).

**Tables**

Table 1. Chemical composition, in mass% (g/g), of the Raw Materials—OptiKast Clay, BB P6 Carbon, and White Alumina—and 1104/1123 FBSR Bed Product and 1125 FBSR Filter Fines. .....37

Table 2. Results of XANES spectra fitting for pilot-scale FBSR NAS granular product. .....37

**Table 1.** Chemical composition, in mass% (g/g), of the Raw Materials—OptiKast Clay, BB P6 Carbon, and White Alumina—and 1104/1123 FBSR Bed Product and 1125 FBSR Filter Fines.

| Oxide | OptiKast Clay | BB P6 Carbon Ash | White Alumina | 1104/1123 FBSR Bed Product | 1125 FBSR Filter Fines |
|---|---|---|---|---|---|
| $Al_2O_3$ | 42.89 | 0.30 | 100.14 | 32.50 | 34.77 |
| CaO | 0.03 | 67.50 | 0.14 | 2.31 | 1.78 |
| $Cr_2O_3$ | - | - | 0.01 | 0.12 | 0.10 |
| $Cs_2O$ | - | - | - | 0.00 | 0.00 |
| $Fe_2O_3$ | 0.37 | 0.43 | 0.14 | 0.27 | 0.25 |
| $K_2O$ | 0.07 | 3.31 | 0.00 | 0.30 | 0.31 |
| MgO | 0.02 | 2.45 | 0.02 | 0.07 | 0.06 |
| $Na_2O$ | 0.03 | 0.19 | 0.01 | 20.22 | 22.24 |
| $P_2O_5$ | 0.05 | 1.05 | 0.02 | 0.45 | 0.45 |
| $ReO_4$ | - | - | - | 0.005 | 0.005 |
| $SO_3$ | - | 0.67 | 0.02 | 0.61 | 0.96 |
| $SiO_2$ | 52.73 | 1.50 | 0.86 | 35.73 | 43.00 |
| $TiO_2$ | 1.77 | 0.02 | 0.02 | 1.18 | 1.27 |
| Cl | - | - | - | 0.13 | 0.10 |
| F | - | - | - | 0.10 | 0.10 |
| I | - | - | - | 0.00 | 0.00 |
| $NO_2$ | | 27.00 | | 0.00 | 0.00 |
| $NO_3$ | - | - | - | 0.01 | 0.01 |
| $PO_4$ | - | - | - | - | - |
| $SO_4$ | - | - | - | - | - |

**Table 2.** Results of XANES spectra fitting for pilot-scale FBSR NAS granular product.

| $KReO_4$ | p[a] | $ReO_4^-$-sodalite | p[a] |
|---|---|---|---|
| 0.3±0.3 | 0.390 | 0.7±0.3 | 0.018 |

[a]p is the probability that the improvement to the fit due to including this component is due to random error (noise). If $p < 0.05$, the improvement to the fit due to including this component is greater than two standard deviations of the component.

Appendix 1: Supplemental Information – Geochemical Calculations

The thermodynamic data for nepheline ($NaAlSiO_4$) is well-established, and the calculated log *K* and solubility are close. After comparing calculations with multiple thermodynamic data sources, we chose the reaction from llnl.dat, which came with came with PHREEQC (Parkhurst and Appelo, 1999). The nepheline dissolution reaction is

$$NaAlSiO_4 + 4H^+ \rightleftharpoons Na^+ + Al^{3+} + H_4SiO_4 \tag{6}$$

with log *K* = 13.8006 and temperature function (Parkhurst and Appelo, 1999)

$$\log K = A_1 + A_2 T + \frac{A_3}{T} + A_4 \log T + \frac{A_5}{T^2} + A_6 T^2 \tag{7}$$

with the coefficient of -24.856, $-8.8171\times10^{-3}$, 8565.3, 6.0904, and -227860.0.

The thermodynamic data for nosean was measured and is reported in Lilova et al. (in review). The nosean dissolution reaction is

$$Na_8(AlSiO_4)_6(SO_4)_2 + 24H^+ \rightleftharpoons 8Na^+ + 6Al^{3+} + 6H_4SiO_4 + SO_4^{2-} \tag{8}$$

with a log *K* = 127.22 and $\Delta H$ = -1075.7 kJ/mol. These results resulted in unrealistically high solubility values for nosean. This is because the entropy (S0) data for nosean was not available, and we attempted to use the entropy for nepheline ($\Delta S$ = 124.4 J/mol K) as an approximation for nosean ($\Delta H$ = 124.4 × 6 = 746.4 J/mol K). This entropy value is less than the value measured Cl-sodalite ($\Delta S$ = 848.08 J/mol·K) and Re-sodalite (1190.76 J/mol·K). As a result of this, the log *K* and $\Delta H$ for Cl-sodalite was used as an approximation for nosean. The temperature dependence of the log *K* was corrected using the Van't Hoff equation

$$\log K = \log K_0 + \left(\frac{\Delta H}{2.3R}\right)\left(\frac{1}{T} - \frac{1}{T_0}\right) \tag{9}$$

The thermodynamic data for Re-sodalite was measured and is reported in Pierce et al. (in review). The Re-sodalite dissolution reaction is

$$Na_8(AlSiO_4)_6(ReO_4)_2 + 24H^+ \rightleftharpoons 8Na^+ + 6Al^{3+} + 6H_4SiO_4 + 2ReO_4^- \tag{10}$$

with log *K* = 34.81 and $\Delta H_r$ = -871.33 kJ/mol. Temperature dependence of the log *K* was determined using Eqn. (9).

Each of the aforementioned thermodynamic reactions was added to the phreeqc.dat database and PHEEQC (Parkhurst and Appelo, 1999) version 3 was used for the geochemical calculations. For amorphous silica [$SiO_2$(am)] and chalcedony solubility calculations as a function of pH, the thermodynamic data for $SiO_2$(am) and chalcedony in the PHREEQC database was used.

## DISCLAIMER

This document was prepared as an account of work sponsored by the United States Government. While this document is believed to contain correct information, neither the United States Government nor any agency thereof, nor the Regents of the University of California, nor any of their employees, makes any warranty, express or implied, or assumes any legal responsibility for the accuracy, completeness, or usefulness of any information, apparatus, product, or process disclosed, or represents that its use would not infringe privately owned rights. Reference herein to any specific commercial product, process, or service by its trade name, trademark, manufacturer, or otherwise, does not necessarily constitute or imply its endorsement, recommendation, or favoring by the United States Government or any agency thereof, or the Regents of the University of California. The views and opinions of authors expressed herein do not necessarily state or reflect those of the United States Government or any agency thereof or the Regents of the University of California.